CALPHAD: Computer Coupling of Phase Diagrams and Thermochemistry 72 (2021) 102212

Contents lists available at ScienceDirect

Calphad

journal homepage: http://www.elsevier.com/locate/calphad

TAF-ID: An international thermodynamic database for nuclear fuels applications

C. Guéneau [a,*], N. Dupin [b], L. Kjellqvist [c], E. Geiger [d], M. Kurata [e], S. Gossé [a], E. Corcoran [f], A. Quaini [a], R. Hania [g], A.L. Smith [h], M.H.A. Piro [d], T. Besmann [i], P.E.A. Turchi [j], J.C. Dumas [k], M. J. Welland [l], T. Ogata [m], B.O. Lee [n], J.R. Kennedy [o], C. Adkins [o], M. Bankhead [p], D. Costa [q]

[a] Université Paris-Saclay, CEA, Service de la Corrosion et du Comportement des Matériaux dans leur Environnement, Gif-sur-Yvette, 91191, France
[b] Calcul Thermodynamique, Orcet, France
[c] Lövsjö 205, Överhörnäs, 894 93, Sweden
[d] Ontario Tech University, Ontario, Canada
[e] Japan Atomic Energy Agency, Tokai-mura, Ibaraki, 319-1195, Japan
[f] Department of Chemistry and Chemical Engineering, Royal Military College of Canada, Kingston, Canada
[g] Nuclear Research and Consultancy Group, P.O. Box 25, NL-1755 ZG Petten, the Netherlands
[h] Delft University of Technology, Faculty of Applied Sciences, Radiation Science & Technology Department, Mekelweg 15, 2629, JB Delft, the Netherlands
[i] University of South Carolina, Columbia, SC, 29208, USA
[j] Lawrence Livermore National Laboratory, Livermore, CA, 94550, USA
[k] CEA, DES, IRESNE, DEC, Cadarache F-13108 Saint-Paul-Lez-Durance, France
[l] Canadian Nuclear Laboratories, Chalk River, ON, K0J 1J0, Canada
[m] Central Research Institute of Electric Power Industry, Japan
[n] The Korea Atomic Energy Research Institute, Republic of Korea
[o] Idaho National Laboratory, Idaho Falls, ID, 83415, USA
[p] National Nuclear Laboratory, Chadwick House, Warrington, UK
[q] Nuclear Energy Agency, OECD, Boulogne, France

ARTICLE INFO

Keywords:
Nuclear fuels
Thermodynamic modelling
TAF-ID
Calphad
Severe accident
Corium
Irradiated fuels
Oxide fuels
Metallic fuels
Fuel-cladding interaction

ABSTRACT

The Thermodynamics of Advanced Fuels – International Database (TAF-ID) was developed using the Calphad method to provide a computational tool to perform thermodynamic calculations on nuclear fuel materials under normal and off-normal conditions. Different kinds of fuels are considered: oxide, metallic, carbide and nitride fuels. Many fission products are introduced as well as structural materials (e.g., zirconium, steel, concrete, SiC) and absorbers (e.g., B_4C), in order to investigate the thermochemistry of irradiated fuels and to predict their chemical interaction with the surrounding materials. The approach to develop the database and the models implemented in the database are described. Examples of models for key chemical systems are presented. Finally, a few examples of application calculations on severe accidents with UO_2 fuels, irradiated fuel chemistry of MOX and metallic fuels and metallic fuel/cladding interaction show how this tool can be used. To validate the database, the calculations are compared to the available experimental data. A good agreement is obtained which gives confidence in the maturity degree and quality of the TAF-ID database. The working version is only accessible to the participants of the TAF-ID project (Canada, France, Japan, the Netherlands, Republic of Korea, United Kingdom, USA). A public version is accessible by all the NEA countries. The current version contains models on the Am–Fe, Am–Np, Am-O-Pu, Am–U, Am–Zr, C–O–U-Pu, Cr–U, Np–U, Np–Zr, O–U–Zr, Re–U, Ru–U, Si–U, Ti–U, U-Pu-Zr, U–W systems. It is progressively extended with our published assessments. Information on how to join the project is available on the website: https://www.oecd-nea.org/science/taf-id/.

* Corresponding author. , ISAS- Service de la Corrosion et du Comportement des Matériaux dans leur Environnement (SCCME), CEA, Université Paris-Saclay, Bât. 450 SE, F-91191, Gif-sur-Yvette, France.
E-mail address: Christine.gueneau@cea.fr (C. Guéneau).

https://doi.org/10.1016/j.calphad.2020.102212
Received 27 August 2020; Received in revised form 19 October 2020; Accepted 22 October 2020
Available online 11 November 2020

1. Introduction

Under normal operating conditions in Light Water Reactors (LWR), the oxide fuel is exposed to simultaneous conditions of high temperature (1300 K at the center and about 750 K at the rim), irradiation and thermomechanical stresses that lead to significant changes of its microstructure with time and burnup [1]. These changes affect key fuel properties such as thermal conductivity, margin to melting (formation of the first liquid), diffusion, creep, and fission gas release, that have to be well known for a thorough safety assessment of the reactor. With burnup, numerous fission products (FPs) form and the fuel chemical composition changes with time. These fission products are either solubilized into the fuel oxide matrix or precipitate as separated phases [2]. Moreover, the thermal gradient between the center and the periphery of the fuel pellet induces mass transport and segregation of some elements along the temperature gradient. For instance, in LWRs fuels under high burnup conditions, volatile fission products like iodine, cesium and tellurium can migrate from the center to the periphery of the fuel pellet and, in some cases, attack the cladding leading to fuel Pellet Cladding Interaction (PCI) [3]. Also, in fast breeder fuels (mixed oxide of uranium and plutonium (MOX)), that are exposed to higher temperatures (2300 K at the center and about 1000 K at the rim), the volatile fission products (i.e., iodine, cesium, tellurium, molybdenum) can migrate to the periphery of the fuel pellet to form a fission product enriched layer, the so-called JOG (Joint Oxyde Gaine) [4]. In some cases, the fission products can attack the cladding leading to the ROG (Reaction Oxyde Gaine) formation [5].

Fuel performance codes have been developed to simulate the fuel pin behaviour under normal and abnormal operating conditions. Among the different properties that have to be taken into account, the change of the fuel composition with the fission product formation and of its related thermodynamic properties (e.g. heat capacity, oxygen potential, margin to fuel melting, *etc*.) have to be well known and predicted. The incorporation of such changes of the fuel properties in a fuel performance code is important [6].

Even if the fuel is not at equilibrium conditions, thermodynamic calculations on such complex fuel chemical composition are useful to predict locally the phases that can form and how the phase fractions vary with burnup. By coupling thermodynamics to mass diffusion, the thermal transport of elements can be addressed too. Moreover, from these calculations, the partial pressures of the semi-volatile and volatile elements can be calculated to predict fission product release from fuel pins and/or transport to the periphery of the fuel pellet [6,7].

Under accidental conditions, the thermodynamic calculations are of great interest to predict the solid, liquid and gas phases of degraded materials. The most important role is to estimate the phase stability of the molten core materials, so-called "*corium*", at high temperature. In *corium*, a few metallic and oxidic melt layers are considered to be stratified. Again, even if the *corium* is not at equilibrium conditions, the thermodynamic calculations can provide input data of composition and density of these metallic and oxide phases. The improvement of the stratification model at the lower head of the vessel is one major issue for severe accident analysis, including macroscopic variation in *corium* and the heat transfer from *corium* to reactor vessel. In some cases, input thermodynamic data are taken into account in thermal-hydraulics computational codes to predict heat transfer in *corium* pools in severe accident codes [8]. As mentioned above, a fission product chemical database is being developed to model fission product release in severe accident codes and indeed the partial pressures of gaseous species of fission products calculated by a thermodynamic approach are then important parameters. This evaluation is highly important for the analysis of the Fukushima-Daiichi Nuclear Power Plant accident. Also the chemical state of the phases in the *corium* has to be assessed for reprocessing of the fuel. For any normal or abnormal condition, an understanding of the equilibrium states in fuel is essential if we are to bound the uncertainties in fuel behaviour.

The purpose of the Thermodynamics of Advanced Fuels – International Database (TAF-ID) project is to provide a comprehensive thermodynamic database on nuclear fuel materials that can be used with Thermo-Calc [9] or Open Calphad [10] codes to perform a wide range of thermodynamic calculations for different applications of nuclear reactors. The interest in a thermodynamic database was first generated with regard to LWR and CANada Deuterium Uranium (CANDU) fuels, but has now extended to the development of advanced fuels (e.g., oxide, metallic, nitride, carbide) and claddings materials as well (e.g. zirconium alloys, steels, SiC …) for future nuclear reactors, Accident Tolerant Fuels (ATF) and Generation IV systems). It requires the investigation of these advanced fuel thermodynamic properties and its chemical compatibility with new cladding materials in normal and abnormal conditions.

When dealing with such complex chemical systems containing a large number of chemical elements, the Calphad methodology is the most suitable approach to predict thermodynamic properties and phase equilibria [11]. In the Calphad method, thermodynamic equilibrium is calculated for a given amount of chemical elements, temperature and pressure, by minimization of the total Gibbs energy of a closed system. The total Gibbs energy of the system is the sum of the Gibbs energies of all the constituting phases (*i.e.* solid, liquid and/or gas). The Gibbs energy functions of all the phases are assessed as a function of temperature and composition (and pressure for the gas only) by fitting all the available information (thermodynamic and phase equilibria data) using a linear regression method [11].

In a first step, the binary systems are modelled to account for the formation of binary compounds, and solid and liquid solutions. Then, the ternary phase diagrams can be calculated by extrapolation. By experience, it is often necessary to add ternary thermodynamic parameters in case of the existence of ternary compounds or/and to get a good description of the solid/liquid solutions with respect to available experimental data. This kind of database has for instance been developed for steels, Ni, Al, Cu *etc* … based alloys and also for other types of materials like slags, solders, *etc*. Generally, the extrapolation from the binary and ternary systems leads to a good prediction of the phase equilibria and thermodynamic properties of complex systems containing a large number of elements (up to ~30 elements). The advantage of Calphad type databases is that both phase diagrams and all phase thermodynamic properties can be calculated. The aim of this project is to develop such a database for advanced nuclear fuel materials to predict its behaviour in a wide temperature and composition range.

The Thermo-Calc software [9] was used for the development of the TAF-ID database and for all the calculations presented in this paper.

2. TAF-ID project

The TAF-ID project, coordinated by the Organization for Economic Co-operative Development Nuclear Energy Agency (OECD/NEA), started in 2013 [12]. The idea of such an international project came from the ascertainment that several databases on nuclear materials were being developed independently in different countries and that the development of such large databases requires a significant effort by qualified persons with rare expertise. The main idea was to have a concerted effort to launch an international project to create and develop a unique database starting from the existing ones, and to foster exchanges on thermodynamic data and models for nuclear fuel systems.

These databases are briefly described in Table 1. Two commercial software packages are commonly used for the Gibbs energy minimization: Thermo-Calc [9] and FactSage [13]. Depending on the databases, different types of models are used. In the databases on oxide fuels from Canada and the Netherlands, there are mainly stoichiometric compounds [14, 15, 16,17,18] and a few solutions are described for the fluorite oxide phase, in which the dissolution of numerous dissolved fission and activation products is described, and the noble metal phases [16]. In the United States, extended models were

developed to describe mixed oxides (U,Ln)$O_{2\pm x}$ and related phase diagrams with Ln = Pr, La, Nd, Y, Gd, Ce [19,20,21,22,23,24,25,26]. In these databases, not all the solutions (solid and liquid) are modelled for all the systems. Thus, phase diagrams, solid/liquid transitions cannot be calculated for some complex fuel compositions. In the databases developed by France, Japan and USA (LLNL), full Calphad models are introduced that allow the calculation of complete phase diagrams [27,28,29]. Thus, mainly two types of databases exist. Either databases contain many elements but mainly describing stoichiometric compounds and a few solutions or a full Calphad description with less elements but modelling the non-stoichiometry and the solubility of the elements in all the phases.

Within the TAF-ID project, it has been decided to adopt a full Calphad modelling approach for our database in order to provide both phase diagram and thermodynamic data calculations. Furthermore, for the oxide phases, the two sublattice ionic liquid model [30,31] and the Compound Energy Formalism with ionic species [32] were chosen for the liquid and the mixed oxides, respectively. The FUELBASE database [27] developed by CEA (Commissariat à l'Energie Atomique) from 2005 to 2012 was used as a starting point to develop the TAF-ID database, which was progressively extended for five years by introducing either models coming from research and/or databases of the participants of the project, or coming from the open literature. Binary and ternary systems for which no descriptions existed were assessed in the framework of this project.

In the current version of the TAF-ID database (Version 9), different types of fuels are described: oxides $UO_{2\pm x}$, mixed oxides (U,Pu)$O_{2\pm x}$, ThO_2, metallic (U,Pu,Zr), carbide (U,Pu)C, and nitride (U,Pu)N fuels. Binary and ternary oxides containing minor actinides (i.e., Am and Np) are also modelled: AmO_{2-x}, NpO_{2-x}, (Am,Pu)O_{2-x}.

Numerous fission products have been introduced to predict the thermochemistry of irradiated oxide fuels:

- Lanthanoids: Ce, La, Gd, Nd that dissolve in the fluorite oxide matrix;
- Ba, Sr, Mo, Zr that form the so-called "grey phases" of formula (Ba,Sr,Cs)(Zr,U,Pu,Mo)O_3 in the oxide fuels [2];
- Pd, Rh, Ru, Te, Tc that mainly precipitate as metallic phases;
- Cs, Te, I, Ru: semi-volatile and volatile elements that form both gaseous species or/and condensed phases.

To predict the chemical interaction between the fuel and various structural materials, the chemical systems representative for steels (*i.e.* Fe–Cr–Ni), Zr alloys, SiC with liners (*i.e.* Re, W, Ta and Nb), absorber B_4C and concrete (*i.e.* SiO_2–CaO-Fe_xO_y-MgO-Al_2O_3) have been introduced.

The current Version 9 of the TAF-ID database contains the following 42 chemical elements marked in bold in the periodic table in Fig. 1: Ag, Al, Am, Ar, B, Ba, C, Ca, Ce, Cr, Cs, Fe, Gd, H, He, I, La, Mg, Mo, N, Nb, Nd, Ni, Np, O, Pd, Pu, Re, Rh, Ru, Si, Sr, Ta, Tc, Te, Th, Ti, U, V, W, Y and Zr. Of over 820 binary systems, 210 are described in the current version of the database (Fig. 2). Among those systems, 87 binaries were assessed in the framework of the TAF-ID project. The other models for the binaries were taken from the open literature. 76 ternary systems are modelled (Fig. 3), of which 33 were assessed within the TAF-ID project.

In the framework of the project, the database was comprehensively documented in HTML format from which Figs. 1, Figs. 2 and 3 were extracted. It gives information on the models and the crystalline data for the phases. For the systems assessed within the project, the original experimental data used for the assessment are given. Figures comparing calculated and experimental data are presented. In case of a model coming from the literature, the source paper reference is given. In some cases, comparisons between different models are presented in order to provide justification for the selection of the model that was introduced in the database.

A public version of the TAF-ID database is accessible by all OECD/NEA members [12]. This version contains the database files and the documentation for the following systems: Am–Fe, Am–Np, Am-O-Pu, Am–U, Am–Zr, C–O–U-Pu, Cr–U, Np–U, Np–Zr, O–U–Zr, Re–U, Ru–U, Si–U, Ti–U, U-Pu-Zr, U–W. This public version is being progressively extended by adding assessments when published in the open literature. The working version is accessible only by the participants of the TAF-ID project (Canada, France, Japan, the Netherlands, Republic of Korea, United Kingdom, USA). Information on how to join the project is available on the website: https://www.oecd-nea.org/science/taf-id/.

Table 1
Status of the thermodynamic databases developed by the different partners of the TAF-ID project in 2013. "FPs": "Fission Products".

Involved Countries Institutes	Software	Chemical systems	Model
Canada AECL RMC UOIT	*FactSage* *Thermochimica*	Fuel UO_2 + Np, Pu + Coolant H_2O FPs: (Kr), Rb, Sr, Y, Zr, Mo, Tc, Ru, Rh, Pd Te, I, Xe, Cs, Ba, La, Ce, Pr, Nd	302 compounds 17 solutions [14–16]
France CEA	*Thermo-Calc*	Fuel UO_2, MOX + Am,Np, (U,Pu,Zr), (U,Pu)C, (U,Pu)N FPs: Ag, Ba, Cs, I, La, Mo, Nb, Ru, Sr, Te Materials: Concrete, B–C, Fe–Cr–Ni, SiC,Ta, W, V	Solutions 144 binaries 30 ternaries [27,33,34,35,36,37,38,39,40,41,42,43]
Japan JAEA, CRIEPI	*Thermo-Calc*	Metallic fuel: Am-Cd-Ce-Fe-Gd-La-Nd-Np-Pr-Pu-U-Y-Zr Oxide fuel: Pu-Zr-O, Fe–B–C–O	Solutions [28,29]
Netherlands NRG	*FactSage*	Fuel: (U, Pu, Am, Np, Th)-(C, N, O) FPs: Ag, Ba, Br, Ce, Cs, Eu, I, La, Mo, Nb, Nd, Pd, Rb, Ru, Sb, Sn, Sr, Te, Y, Zr Materials: Fe, Ni, Si, Ti, Ta, W, Zn + Na, H, Pb	727 compounds [17,18]
USA ORNL LLNL	*FactSage* *Thermo-Calc*	UO_2 + RE: Pu-U-Gd-Ce-La-O Metallic fuel: Am–Pu, Mo–Pu, Mo–U,Nb–U,Nb–Zr,Pu–U, Ti–U,U–Zr Materials: Be–Cu–Fe–Nb–Ta–Ti–Zr	C1 solution + compounds [19–26] Solutions

A significant success of the project has been the participation of a large number of institutions, with individual priorities, facilities, and funding streams. The formation of a common database creates a standard of accepted potentials useful for future developments by individual groups. Systems may be built from a common reference, which implies consistency between new models. Therefore, new models have added-value in that they readily incorporate into the overall database, and the database as a whole grows coherently through coordination of efforts. A further benefit can be gained in terms of long-term preservation of data. By sharing this critically important data in an open forum, it is preserved for future generations of nuclear scientists to access rather than being held internally where it could be lost when experts leave the industry.

3. Gibbs energy models

The Calphad method is used to derive Gibbs energy functions for all the solid, liquid and gas phases as a function of temperature, composition and pressure [11]. The Gibbs energy functions are referred to ${}^{\circ}H_i^{SER}(298.15)$, the enthalpy of the pure elements at 298.15 K and 1 bar (SER: Standard Element Reference state).

Each phase is described using several sublattices "s_1, s_2 … s_l". In each sublattice, one or several constituents, *i*, are introduced. a_s is the number of sites on each sublattice. The constituent site fraction in each sublattice is denoted by $y_i^{(s)}$.

In case of a stoichiometric compound, there is a single species in each sublattice and the Gibbs energy is expressed as follows:

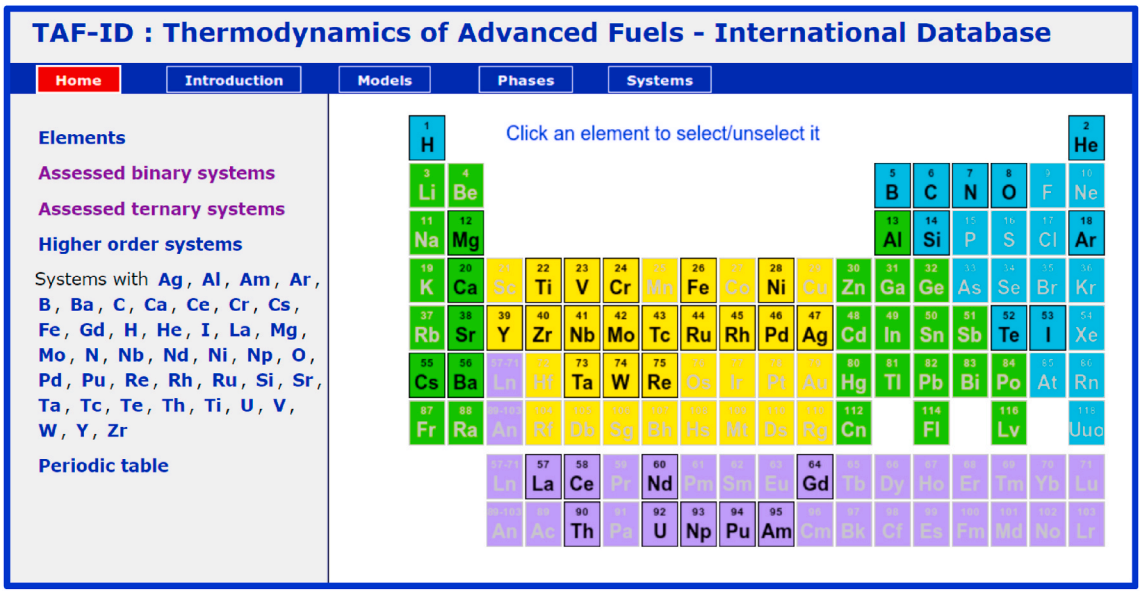

Fig. 1. List of the elements described in the TAF-ID database Version 9, colored in black. Page extracted from the documentation developed within the TAF-ID project.

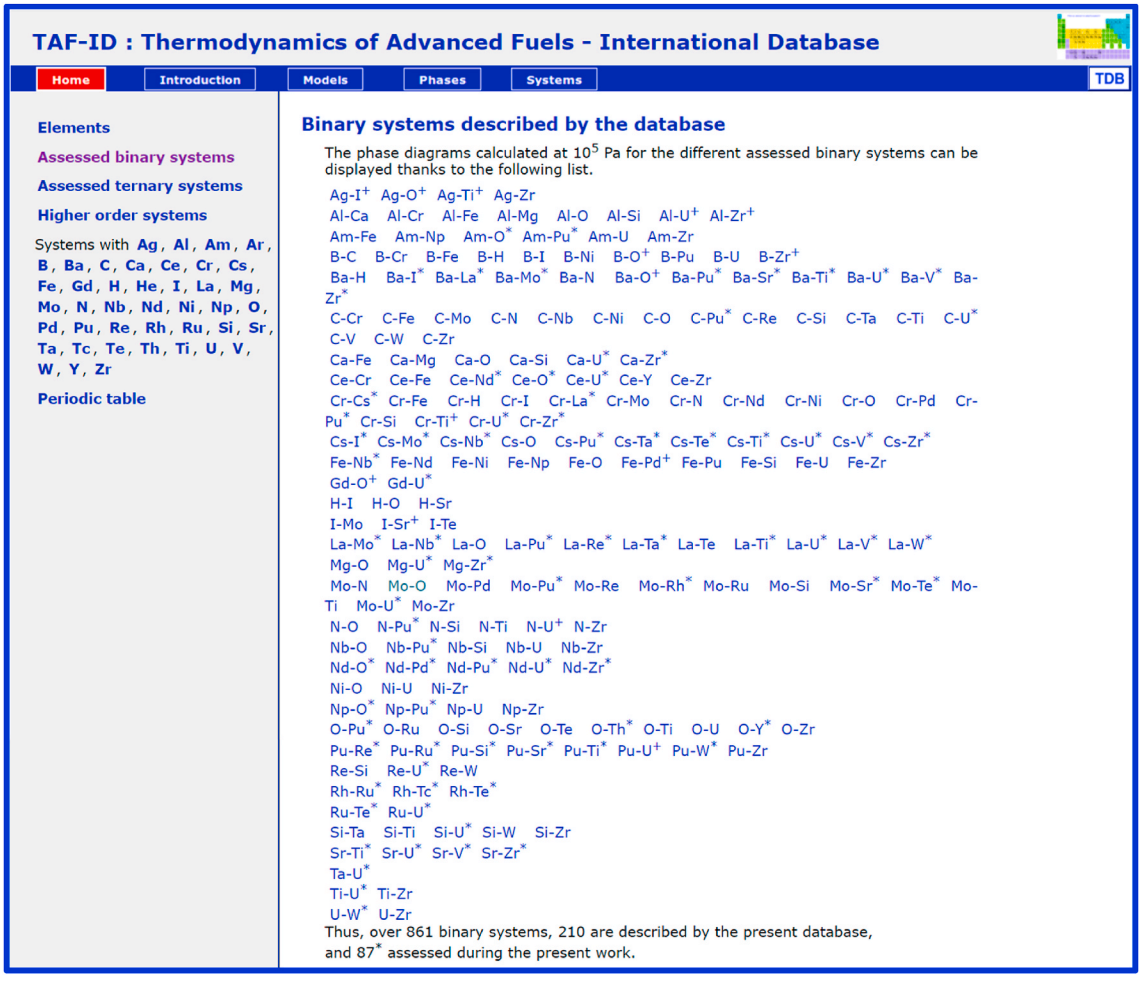

Fig. 2. Binary systems modelled in the TAF-ID database Version 9. Page extracted from the documentation developed within the TAF-ID project.

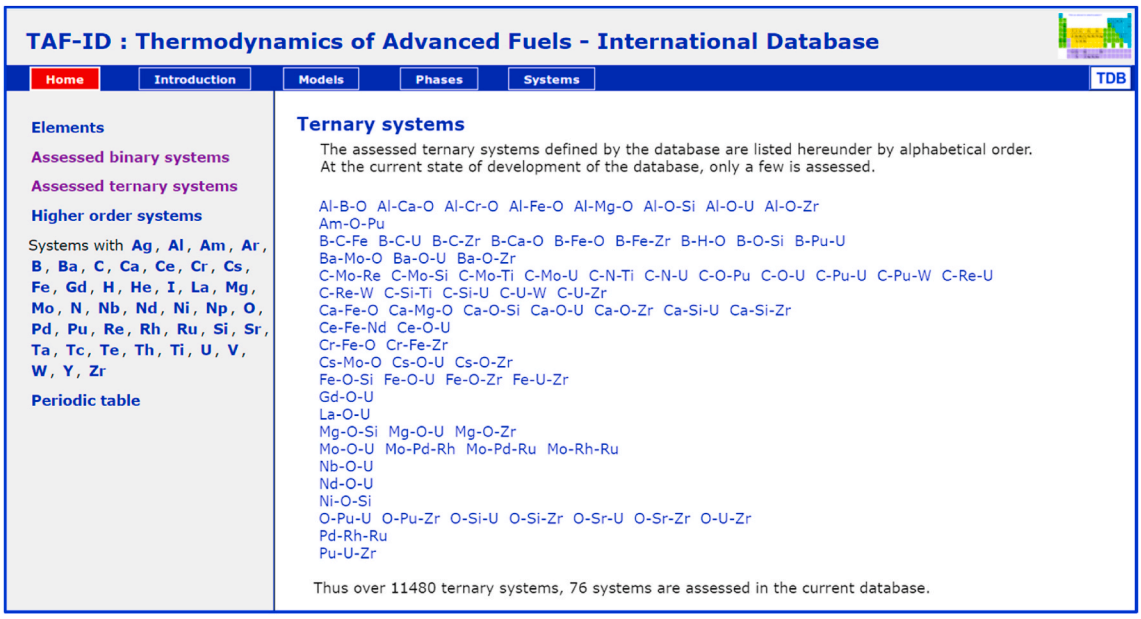

Fig. 3. Ternary systems modelled in the TAF-ID database Version 9. Page extracted from the documentation developed within the TAF-ID project.

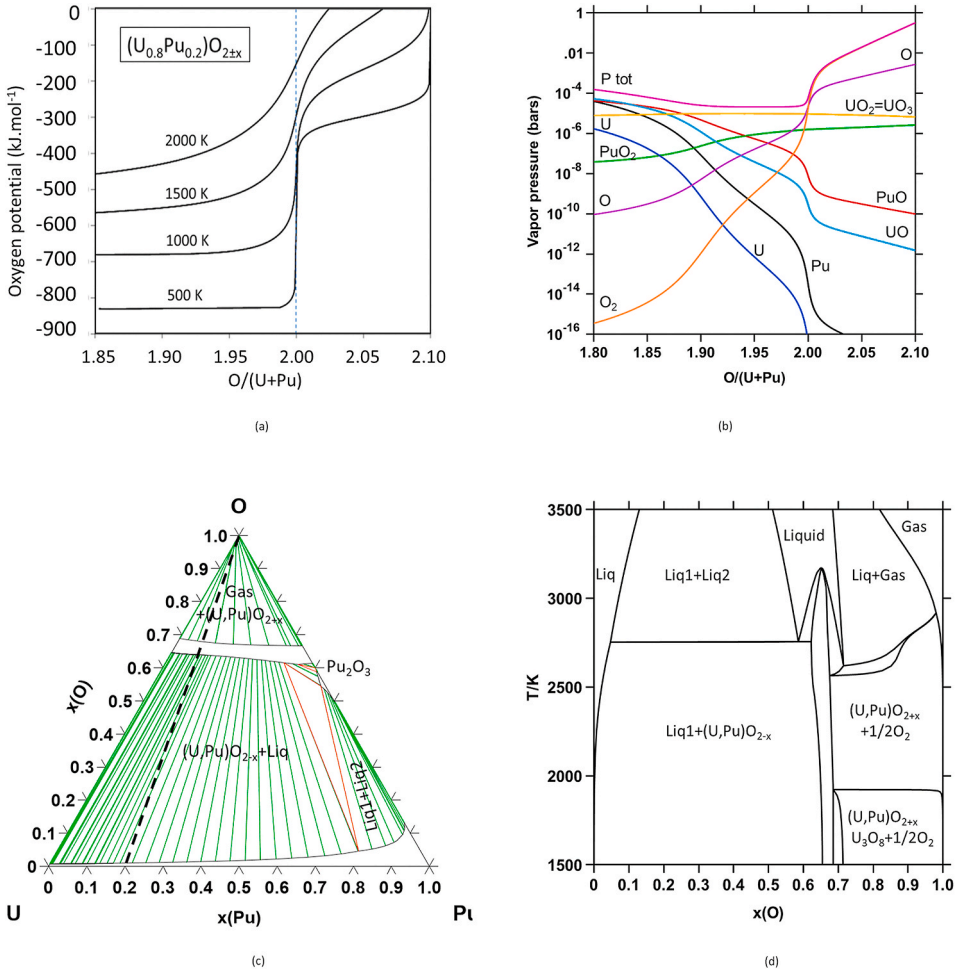

Fig. 4. Calculated (a) oxygen potential of $(U_{0.8}Pu_{0.2})O_{2\pm x}$ as function of O/(U + Pu) ratio at 500, 1000, 1500 and 2000 K; (b) vapor pressure of the gaseous species and total pressure above $(U_{0.8}Pu_{0.2})O_{2\pm x}$ as function of O/(U + Pu) at 2300 K; (c) isothermal section of the U-Pu-O system at 2300 K; (d) isopleth section of the U-Pu-O system with U/Pu = 4 along the composition line reported on the isothermal section (dashed line).

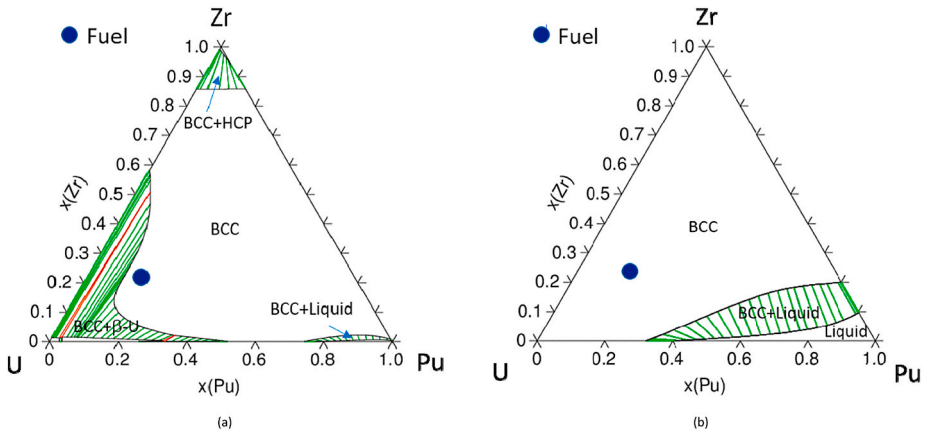

Fig. 5. Calculated U-Pu-Zr isothermal section at (a) 923 K (b) 1123 K.

$$G^{\phi} - \sum a_i^{\phi} \circ H_i^{SER}(298.15) = a + b\,T + c\,T\,lnT + \sum_n d_n\,T^n \tag{1}$$

with T, the temperature, a_i^{ϕ}, the site numbers on the sublattices, and $n = 2, 3, -1$. In some cases, other values for n are used.

In a more general approach, using the Compound Energy Formalism, the Gibbs energy of the phases is expressed as the sum of the following three terms:

$$G_m^{\phi} - \sum x_i^{\phi} \circ H_i^{SER}(298.15) = {}^{srf}G_m - T\,{}^{cnf}S_m + {}^{E}G_m \tag{2}$$

$${}^{srf}G_m = \sum_{I_0} P_{I_0}(Y) \circ G_{I_0} \tag{3}$$

$${}^{cnf}S_m = -R \sum_{s=1}^{n} a_s \sum_{i=1}^{n_s} y_i^{(s)} ln\left(y_i^{(s)}\right) \tag{4}$$

$${}^{E}G_m = \sum_{I_1} P_{I_1}(Y) L_{I_1} + \sum_{I_2} P_{I_2}(Y) L_{I_2} + \ldots \tag{5}$$

In the reference term, ${}^{srf}G_m$, I_0 is a compound formed by considering a single constituent in each sublattice, corresponding to a compound end member. $P_{I_0}(Y)$ is the product of the constituent site fractions related to I_0. $^{\circ}G_{I_0}$ is the Gibbs energy of formation of the compound. I_0.

In the configurational entropy term, ${}^{cnf}S_m$, R is the gas constant, and the first sum is over all sublattices and the second one, over all constituents on each sublattice.

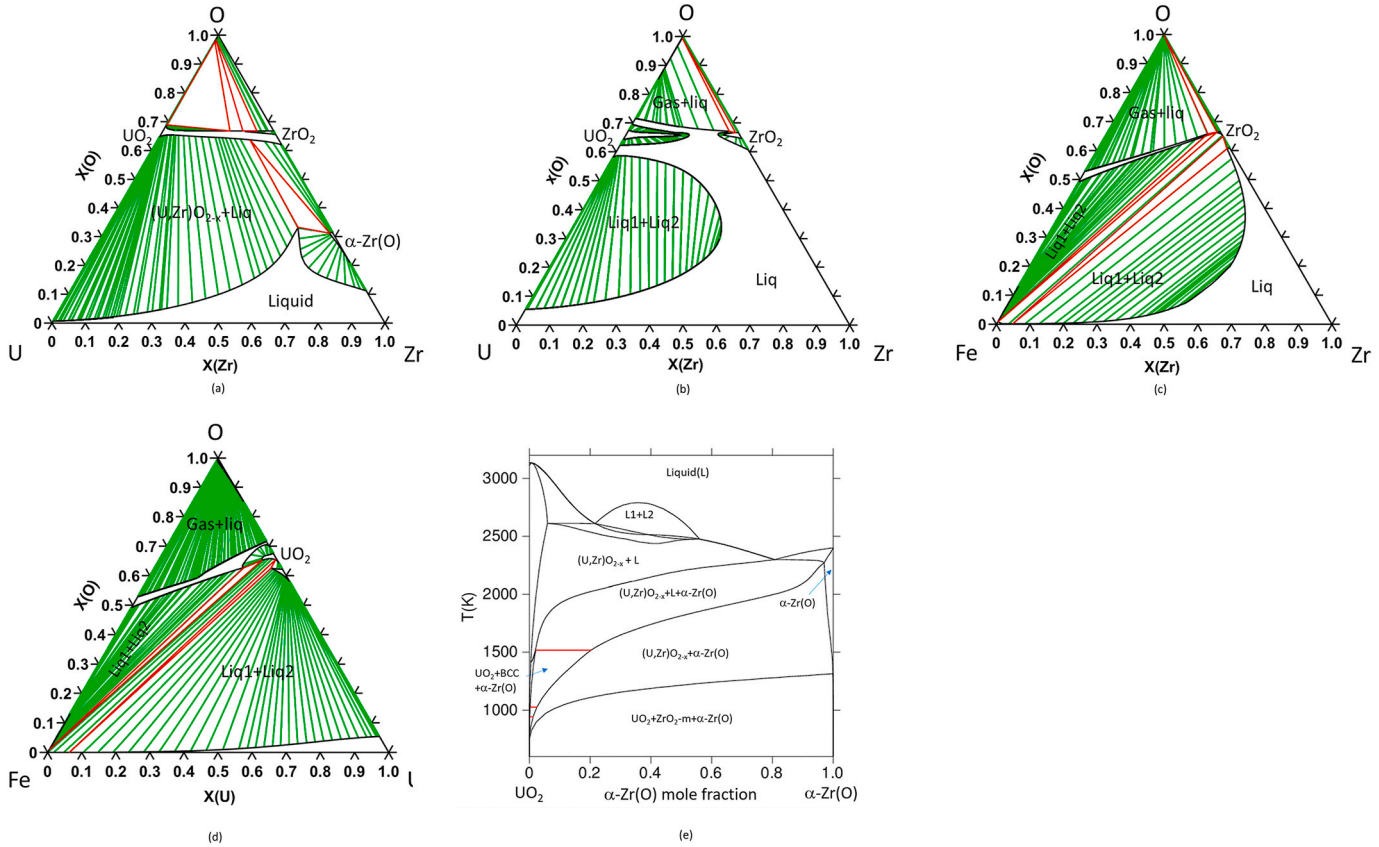

Fig. 6. Calculated isothermal sections (a) U–O–Zr at 2273 K, (b) U–O–Zr at 2873 K; (c) Fe–O–Zr at 2873 K; (d) Fe–O–U at 2873 K; (e) UO_2-α-Zr(O) isopleth using the model of Quaini et al. [12,45].

Table 2
Comparison between calculated and experimental compositions in w. % of the metal and oxide liquid phases for corium A1 and E2 [48], for ISABEL1 [49] and for MA1 and MA2 MASCA tests [51].

Experiment	Composition				
Corium A1 2900 K	Overall	Oxide		Metallic	
w. %		Exp.	Calc.	Exp.	Calc.
U	60.4	67.3	67.2	45.6	43.7
Zr	17.3	17.8	19.7	16.4	11.4
Fe	9.7	1.8	0.4	26.6	32.4
Ni	1.5	0.3	/	4.1	5.2
Cr	2.2	0.5	0.16	5.9	7.2
O	8.9	12.3	12.5	1.4	0.1
Phase w. %		68	71	32	29
Corium E2 2900 K	Overall	Oxide		Metallic	
w. %		Exp.	Calc.	Exp.	Calc.
U	30	61	60.55	<0.6	0.1
Zr	9.3	19.8	18.8	<0.4	0.25
Fe	37.9	1.2	2.9	70	72.1
Ni	5.4	<0.2	/	12	10.7
Cr	9.3	2.2	1.7	16.2	16.7
O	8.1	15.1	16.0	<0.2	0.3
Phase w. %		50	49	50	51
ISABEL1 3000 K	Overall	Oxide		Metallic	
w. %		Exp.	Calc.	Exp.	Calc.
U	81	76.2	88.1	86.45	80.0
Zr	10.6	12.6	2.7	5.2	11.6
Fe	6.8	0.6	0.2	7.3	7.7
O	1.6	10.5	9.06	1.05	0.6
Phase mol. %		~10	18	~90	82
MA1 2800 K	Overall	Oxide		Metallic	
w. %		Exp.	Calc.	Exp.	Calc.
U	61.96	67.22	68.3	43.2	37.4
Zr	16.36	18.0	18.3	10.5	8.8
Fe	7.85	1.3	0.35	31.2	37.15
Cr	2.29	0.3	0.15	9.4	10.65
Ni	1.26	0.1	/	5.4	6.2
O	10.28	13.1	12.9	0.3	/
MA2 2800 K	Overall	Oxide		Metallic	
w. %		Exp.	Calc.	Exp.	Calc.
U	59.0	64.4	61.3	20.2	17.2
Zr	17.61	19.3	23.6	5.5	5.4
Fe	7.47	1.3	0.4	51.8	53.55
Cr	2.18	0.4	0.2	15.0	15.6
Ni	1.14	0.3	/	7.2	8.2
O	10.28	13.1	14.5	0.3	/

The third term in equation (2) is the excess Gibbs energy term, ${}^{E}G_{m}$, expressed as the sum over the possible interaction parameters between the constituents on the sublattices, L_{I_i}, which can have a dependence on temperature. I_1 refers to a component array of the first order that in one sublattice contains two components but only one in each of the remaining sublattices.

Examples of models developed with the CEF model can be found in the public version of the database [12] and also in the related published papers [29,28,35,36,37,38,39,40,41,42,43,44,45].

As the database contains many metal-oxygen systems, specific models for those systems are used.

For the solid oxide phases, in most of the cases, ionic constituents are introduced in the sublattices. As an example, the model used to describe $UO_{2\pm x}$, PuO_{2-x} and $(U,Pu)O_{2\pm x}$ from Guéneau et al. [38] was extended as follows:

$(Al^{+3}, Am^{+3}, Am^{+4}, Ba^{+2}, Ca^{+2}, Ce^{+3}, Ce^{+4}, Gd^{+3}, La^{+3}, Mg^{+2}, Nb^{+5}, Nd^{+3}, Np^{+3}, Np^{+4}, Pu^{+3}, Pu^{+4}, Sr^{+2}, Th^{+4}, U^{+3}, U^{+4}, U^{+5}, Zr^{+2}, Zr^{+4})$ $(O^{-2},Va)_2$ (O^{-2},Va).

where the vacancies "Va" allow a variation of the site occupancy of the two sublattices containing oxygen. The first sublattice is the site for the metallic cations, the second sublattice represents the normal site for oxygen anions whereas the third one contains interstitial oxygen anions in the fluorite structure. With this three sublattice model, it is possible to describe both hypo $(M_1^{+\nu 1}\ M_2^{+\nu 2}, \ldots)$ $(O^{-2},Va)_2$ (Va) and hyper-stoichiometric $(M_1^{+\nu 1}\ M_2^{+\nu 2}, \ldots)$ $(O^{-2})_2$ (O^{-2},Va) oxygen compositions for the different mixed oxides. Both oxygen vacancies and interstitials can be present at very high temperature, in stoichiometric UO_2 for instance, constituting disorder in the system. The Gibbs energy of the fluorite phase is described by equation (2).

The liquid phase is described using the ionic two sublattice model containing the following species [30,31]:

$(Ag^{+}, Al^{+3}, Am^{+3}, Ba^{+2}, Ca^{+2}, Ce^{+3}, Cr^{+2}, Cs^{+}, Fe^{+2}, Gd^{+3}, La^{+3}, Mg^{+2}, Mo^{+4}, Nb^{+2}, Nd^{+3}, Ni^{+2}, Np^{+4}, Pd^{+2}, Pu^{+3}, Re^{+4}, Rh^{+3}, Ru^{+4}, Si^{+4}, Sr^{+2}, Ta^{+2}, Tc^{+4}, Th^{+4}, Ti^{+2}, Ti^{+4}, U^{+4}, V^{+2}, W^{+4}, Zr^{+4})_P$ $(AlO_2^{-}, I^{-}, O^{-2}, SiO_4^{-4}, MoO_4^{-2}, Va^{-Q}, B, B_2O_3, C, CeO_2, CrO_{3/2}, CsO_2, Cs_2Te, FeO_{3/2}, I_2, MoO_3, NbO_2, NbO_{5/2}, N, O, Te, PuO_2, SiN_{4/3}, SiO_2, Si_2Te_3, TeO_2, UN)_Q$

The first sublattice contains cations and the second one, anions, neutral constituents and charged vacancies denoted "Va^{-Q}". To ensure electroneutrality, the site numbers P and Q are equal to the average charge on the opposite sublattice as follows:

$$P = \sum_j \nu_j\, y_{A_j} + Q\, y_{Va} \tag{6}$$

$$Q = \sum_i \nu_i\, y_{C_i} \tag{7}$$

where $y_i$and ν_i denote respectively the site fraction and the charge of the constituent i (A for an anion, C for a cation and B for a neutral species). The sum of the constituent fractions on each sublattice is unity. Electroneutrality of the phase is maintained by varying P and Q with the composition via the fraction of charged vacancies. This model allows describing purely metallic liquids (with only charged vacancies in the second sublattice) up to fully oxidized liquid phases (with very low vacancy fractions). Different ionic degrees can be described by introducing ionic and neutral species. Using this model, the Gibbs energy function of the liquid is:

$$G^{liq} = {}^{G^{liq}_{ref}+G^{liq}_{id}+G^{liq}_{ex}} \tag{8}$$

$$G^{liq}_{ref} = \sum_C \sum_A y_C\, y_A\, {}^{\circ}G^{liq}_{(C)(A)} + Q\, y_{Va} \sum_C y_C\, {}^{\circ}G^{liq}_{C} + Q \sum_B y_B\, {}^{\circ}G^{liq}_{B} \tag{9}$$

$$G^{liq}_{id} = RT\left[P\sum_C y_C \ln y_C + Q\left(\sum_A y_A \ln y_A + y_{Va}\ln y_{Va} + \sum_B y_B \ln y_B\right)\right] \tag{10}$$

$$\begin{aligned} G^{liq}_{ex} = {} & \sum_{C_1}\sum_{C_2}\sum_{A} y_{C_1}\, y_{C_2}\, y_A\, L^{liq}_{(C_1,C_2)(A)} + \sum_{C_1}\sum_{C_2} y_{C_1}\, y_{C_2}\, y_{Va}^2\, L^{liq}_{(C_1,C_2)(Va)} \\ & + \sum_{C}\sum_{A_1}\sum_{A_2} y_C\, y_{A_1}\, y_{A_2}\, L^{liq}_{(C)(A_1,A_2)} + \sum_{C}\sum_{A} y_C\, y_A\, y_{Va}\, L^{liq}_{(C)(A,Va)} \\ & + \sum_{C}\sum_{A}\sum_{B} y_C\, y_A\, y_B\, L^{liq}_{(C)(A,B)} + \sum_{C}\sum_{B} y_C\, y_B\, y_{Va}\, L^{liq}_{(C)(Va,B)} + \sum_{B_1}\sum_{B_2} y_{B_1}\, y_{B_2}\, L^{liq}_{(B_1,B_2)} \end{aligned} \tag{11}$$

In the reference term (Equation (9)), ${}^{\circ}G^{liq}_{(C)(A)}$ is the Gibbs energy of $(\nu_C + \nu_A)$ moles of liquid $C\nu_A A\nu_C$, ${}^{\circ}G^{liq}_{C}$ is the Gibbs energy of the liquid phase for the pure element corresponding to the C cation and ${}^{\circ}G^{liq}_{B}$ is the

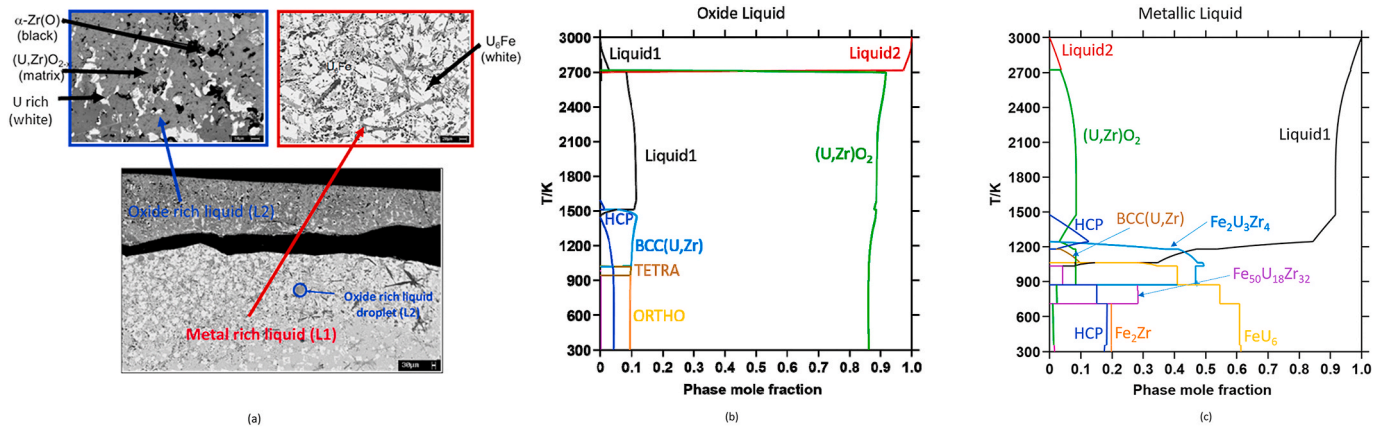

Fig. 7. ISABEL1 test (a) Microstructure of the two quenched liquid phases [49]; (b) and (c): Calculated solidification paths for both oxide and metal liquid phases.

Gibbs energy of the liquid phase for the pure neutral species B. The ideal term in Equation (10) corresponds to the random configurational entropy on each sublattice. In the excess term (Equation (11)), the *L* parameters represent interaction between the different species in each sublattice. The commas separate species interacting in the same sublattice.

For few binary and/or ternary systems, use of atomic scale computational methods (e.g. Density Functional Theory [DFT] coupled with a statistical model) was very useful to calculate thermodynamic data (enthalpy of formation, heat capacity for compounds, mixing enthalpy for solutions) to solve the lack of experimental thermodynamic data [37,44]. This coupling between Calphad/DFT approaches shall be more systematically applied in the future to improve the quality of the database.

4. Examples of key systems

The most important systems for oxide and metallic fuels as well as for corium applications are presented. Application calculations using these models will be described in section 5.

4.1. U-Pu-O for oxide fuels

The model of the U-Pu-O system [38] allows calculating both phase diagrams and all thermodynamic properties of $UO_{2\pm x}$, PuO_{2-x} and (U,Pu) $O_{2\pm x}$ (MOX) fuels.

As an example, the oxygen potential and the vapor pressure above $(U_{0.8}Pu_{0.2})O_{2\pm x}$, the typical fuel composition for Fast Breeder Reactors (FBR) are calculated as a function of the O/(U + Pu) ratio in Fig. 4 (a) at

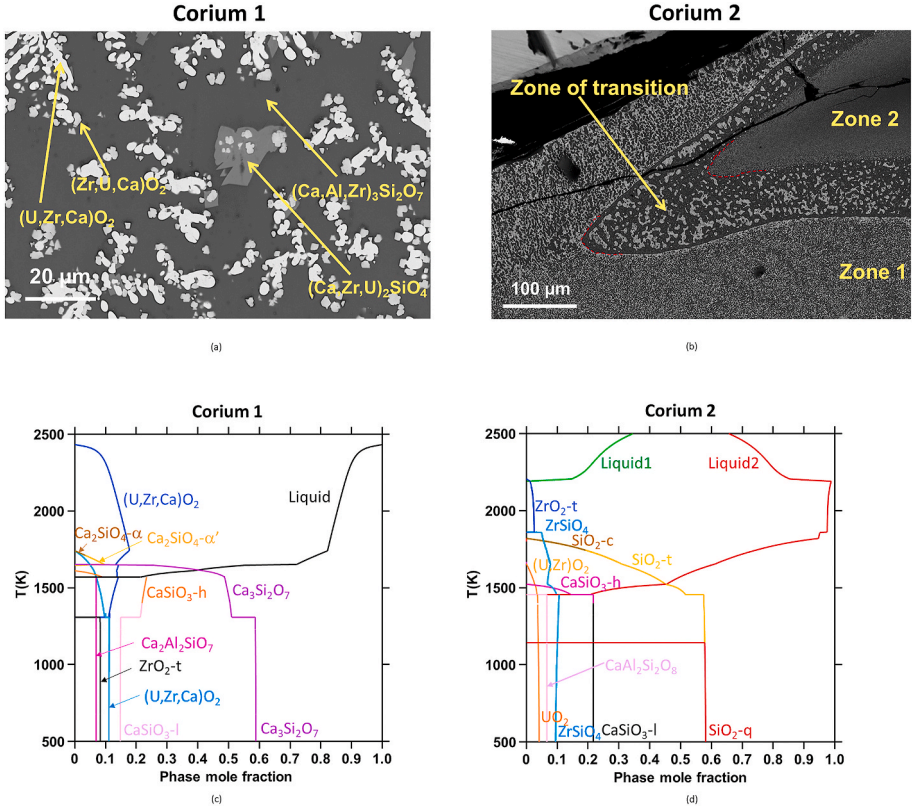

Fig. 8. Microstructure of corium/concrete samples [53] (a) corium 1: single quenched liquid phase; (b) corium 2: two quenched liquid phases (zones 1 and 2), annealed at 2500 K for 30 min and then quenched; (c) calculated solidification path for Corium1; (d) calculated solidification path for Corium 2.

500, 1000, 1500 and 2000 K, and (b) at 2300 K, respectively. The isothermal section at 2300 K and isopleth section with U/Pu = 4 are calculated in Fig. 4 (c) and (d), respectively. All these calculated data can be used for optimizing the experimental conditions (temperature and oxygen partial pressure) of the sintering treatment of MOX fuels in order to adjust the oxygen to metal ratio which has to remain in the range 1.96–1.98. Also the MOX fuel stability can be assessed as a function of temperature and oxygen stoichiometry up to very high temperature.

4.2. U-Pu-Zr for metallic fuels

The model of the Pu-U-Zr system is based on the binary systems published by Kurata [46] for Pu–U, Kurata [47] for Pu–Zr and Quaini et al. [45] for U–Zr. Both phase diagrams and all thermodynamic properties of (U,Pu,Zr) fuels can be calculated with this model. As an example, the isothermal sections are calculated at 923 and 1123 K in Fig. 5(a) and (b), respectively. These temperatures correspond to the minimum and maximum values that can be reached in the metallic fuel pellet, at the periphery and the center, respectively, under normal operating conditions in a fast reactor. A typical composition of the metallic fuel (U-19 wt %Pu-10 wt %Zr) is reported on these diagrams. It can be noted that it is located in the single BCC phase area, far from the stability region of the β-U phase at 923 K and from the liquid phase stability range at 1123 K.

4.3. U–O–Zr–Fe for corium

The U–O–Zr–Fe system is the key system to describe the chemical interaction between UO_2 fuel, Zr alloy cladding and steel vessel that may occur at high temperature during a severe accident. At lower temperature, in operating conditions, the U–O–Zr system is also of paramount interest to describe PCI in high burnup fuels.

The TAF-ID database contains the recent models developed by A. Quaini et al. for U–O–Zr [45], Fe–O–Zr [12] and Fe–O–U [12], and by Kurata et al. for Fe–U–Zr systems [12]. The model of the U–O–Zr system takes into account recent experimental data highlighting the existence of a miscibility gap in the liquid state in this system as well as other data coming from the literature [45]. The miscibility gap comes from the U–O system [33,38]. From the calculated isothermal section of U–Zr–O at 2273 K (Fig. 6(a)), the reaction between UO_2 fuel and Zr cladding leads to the formation of a mixed oxide phase $(U,Zr)O_{2-x}$ in equilibrium with a metallic liquid (U,Zr) containing a small oxygen content. As can be seen in Fig. 6(b), which is at a higher temperature (2873 K), the existence of the miscibility gap leads to the coexistence of two metallic and oxide liquid phases. The zirconium alloy clad can be more or less oxidized. The calculated isopleth in Fig. 6(e) shows the phases forming from the reaction between UO_2 and oxidized Zr (α−Zr(O) or Hexagonal Closed Packed (HCP) phase containing 30 at. % O). At very high temperatures, the miscibility gap in the liquid state is also found to be stable. The composition of the liquid phases in equilibrium in the miscibility gap do not lie in this isopleth section. The liquid compositions are shown at 2873 K by the calculated tielines in Fig. 6(b). As can be seen in Fig. 6(c) and (d), the miscibility gap in the liquid state also exists in both Fe–O–Zr and Fe–O–U systems but no experimental data exist on its extent. During a severe accident, when the corium (UO_2 + Zr more or less oxidized) reacts with the steel (the cladding and other structural components), iron will mainly go in the metallic liquid phase (U,Zr,O). In such a case, the exact compositions of both liquid phases can be calculated with the present model.

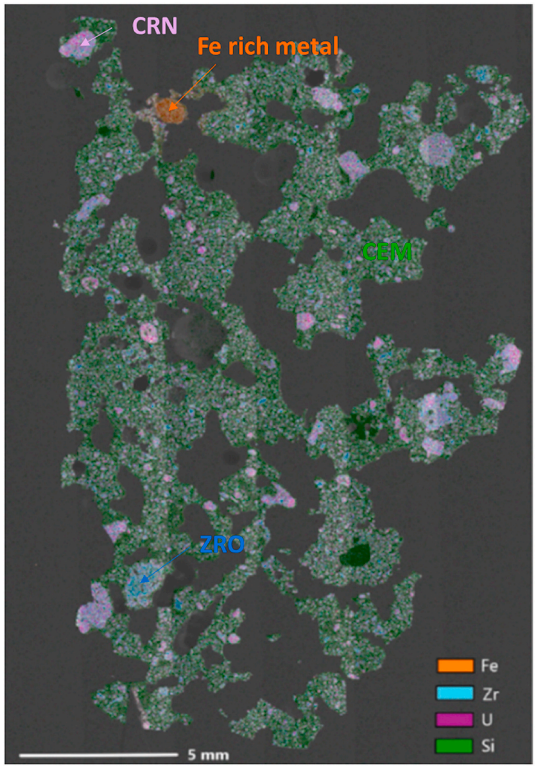

Fig. 9. Microstructure of sample 4 after the VF-U1 VULCANO test [54]. CRN: Corium Rich elements Nodule, CEM: Concrete Elements rich Matrix, ZRO: Zirconium Rich Object.

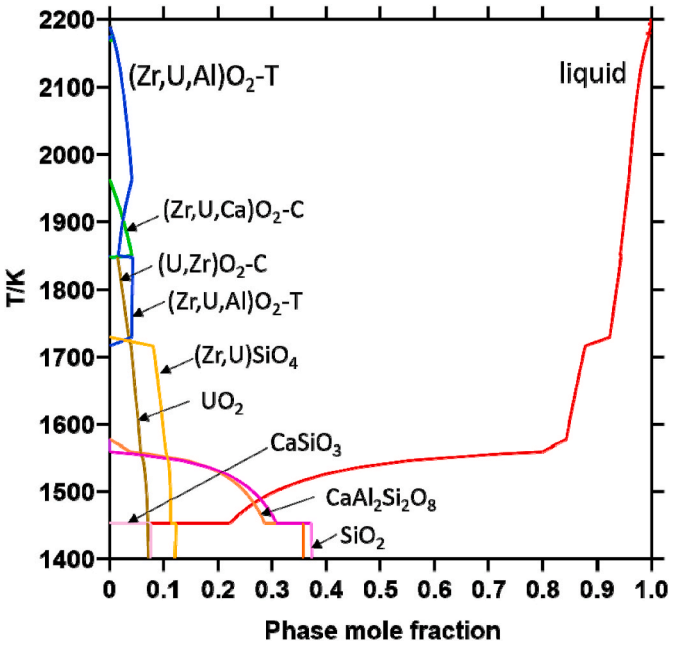

Fig. 10. Calculated solidification path of liquid#1 phase

5. Validation by calculation applications

Examples of calculations performed using the TAF-ID database are presented in this section for different applications: severe accident (in-vessel and ex-vessel corium) for LWR reactors, irradiated MOX and metallic fuel chemistry, metal Fuel/Clad Chemical Interaction (FCCI) for fast reactors. The calculations are compared with the available experimental data.

5.1. Severe accident analyses

5.1.1. In-vessel corium

As mentioned previously, with the incorporation of steel coming

from the vessel into the (UO_2,Zr) *corium*, the steel components Fe, Cr and Ni go into the metallic phase. Depending on the quantity of dissolved steel and on the oxidation rate of the Zr alloy cladding, two different configurations of the *corium* relocation in the steel vessel can be expected: the reference one where the metallic liquid layer is above the oxide melt, and the second configuration, in which a uranium metal liquid phase can relocate to the bottom of the steel vessel below the oxide corium while a steel rich liquid phase remains at the surface of the *corium*. As the highest heat flux is at the interface between the steel vessel and the metallic liquid, one can expect an increase in the risk of vessel damage in the second inverse configuration where the metallic liquid layer at the surface is thinner than in the reference configuration. The inversed configuration can occur due to the existence of a miscibility gap in the liquid state in the U–Zr–O system (see Section 4.3). This example illustrates the importance of a detailed reliable thermodynamic model of such complex systems to correctly predict the phenomenology of the chemical interaction between materials at very high temperatures. In accident conditions similar to that of Fukushima-Daiichi, the lower head of the vessel is likely to fail before complete stratification. The intermediate stage at lower temperatures (i.e. metallic liquid and solid oxide) is also very important. Currently, a thermodynamic approach is the only method to predict these intermediate stages.

The thermodynamic calculations are compared to analytical tests performed by Hofmann [48] and by Guéneau et al. [49]. In the experiments by Hofmann (CORIUM A1 and E2), the components UO_2, Zr and steel were molten by induction heating in a ThO_2 crucible whereas in the ISABEL1 test by Guéneau et al. the materials were melted by electron bombardment. In both experiments, two oxide and metal liquid phases were obtained. The calculated compositions of both oxide and metal liquid phases are compared to the experimental data from Hofmann and Guéneau in Table 2. An overall good agreement is obtained between the calculations and experimental data, although the Fe and Zr content in the liquid phases are not always well reproduced. This could be explained by the fact that there is no experimental data on the miscibility gap in the Zr–Fe–O and U–Fe–O sub-systems. The thermodynamic description of the liquid phases for the in-vessel *corium* could be improved by further investigations of the miscibility gap in these two key sub-systems.

The microstructures of both quenched liquid phases in the ISABEL1 test are shown in Fig. 7(a). The solidification paths of both liquid phases for the ISABEL1 test are calculated in Fig. 7(b) and (c). Fig. 7(b) shows that during cooling, different solid phases form from the oxide liquid: the mixed oxide (U,Zr)O_2 (~90 mol. %) and the BCC (U,Zr) and HCP (α-Zr(O)) metallic solid solutions. This is in agreement with the microstructure of the oxide rich quenched liquid (Fig. 7(a)) where the main phase is the mixed oxide (U,Zr)O_2. The black α-Zr(O) and white precipitates enriched in uranium are present in minor amounts.

Fig. 7(c) shows the more complex solidification path of the metallic liquid phase. At low temperatures, the predominant phase is FeU_6, which is in agreement with the quenched microstructure where the white areas correspond to this major phase. The minor phases found experimentally in this region are: (U,Zr)O_2, Fe_2(U,Zr), α-Zr(O) (or HCP), $Fe_1U_1Zr_1$ and $Fe_5U_2Zr_3$ [49]. The results from the calculations (Fig. 7(c)) are in good agreement with these data, the composition of $Fe_1U_1Zr_1$ being close to the one of $Fe_2U_3Zr_4$.

A considerable experimental campaign was carried out in frame of the MASCA program (OECD/NEA joint project on in-vessel phenomena during a severe accident) [50]. Compared to the previous analytical experiments, these tests involve large masses of components, large temperature gradients and slow cooling rate of the samples. However the comparison between the thermodynamic calculations for the MA1 and MA2 tests in which stratification phenomena of the *corium* molten pool were investigated, leads also to an overall good agreement.

Table 3
Elemental quantities considered for the irradiated (U,Pu)O_2 Phénix fuel sample compositions – FP yields given in Ref. [58] normalized to 2.00 × 10^{-2} for 1 % FIMA in burnup. Some of the fission products (in parenthesis) have been grouped with a representative fission product element.

Element	1 % FIMA [56]	3.8 % FIMA Calc. Darwin	7.0 % FIMA Calc. Darwin	11.2 % FIMA Calc. Darwin
He (+Xe + Kr)	2.6305E-3	9.996E-3	1.841E-2	2.946E-2
Cs (+Rb)	2.1687E-3	8.241E-3	1.518E-2	2.429E-2
I (+Br)	1.8072E-4	6.867E-4	1.265E-3	2.024E-3
Te (+Se + Sb)	3.7149 E−4	1.4116E-3	2.6004E-3	4.1606E-3
Ba (+Sr)	1.0442E-3	3.9679E-3	7.3092E-3	1.1695E-2
Zr (+Nb)	1.9478E-3	7.402E-3	1.363E-2	2.182E-2
Mo	2.1386E-3	8.127E-3	1.497E-2	2.395E-2
Ru	2.2088E-3	8.394E-3	1.546E-2	2.474E-2
Rh	5.8233E-4	2.213E-3	4.076E-3	6.522E-3
Tc	5.5221E-4	2.098E-3	3.865E-3	6.185E-3
Pd (+Ag + Cd + In + Sn)	1.6968E-3	6.4478E-3	1.1878E-2	1.9004E-2
Ce (+Pr)	1.6265E-3	6.181E-3	1.139E-2	1.822E-2
La (+Y + Nd)	2.3092E-3	8.7751E-3	1.6165E-2	2.5863E-2
Gd (+Pm+ Sm + Eu)	5.6225E-4	2.1365E-3	3.9357E-3	6.2972E-3
O	1.982	1.982	1.979	1.983
U	0.79200	0.77249	0.74930	0.70472
Pu	0.19800	0.18951	0.18070	0.18328

5.1.2. *Ex-vessel corium*

For ex-vessel *corium* compositions, very few phase diagram data exist. Liquidus and solidus temperatures of *corium*/concrete mixtures for different types of concrete (limestone, siliceous, *etc* …) were measured by Roche et al. [52] but for several samples, the liquidus temperature could not be clearly detected and no microstructural analysis of the samples is available. New measurements would be needed to form a more definitive understanding. Calculations are performed on: i) well controlled heat treatments of (UO_2–ZrO_2)/(SiO_2–CaO–Al_2O_3) compositions with two CaO and SiO_2 rich concrete compositions [53], and ii) VULCANO corium concrete interaction test VF-U1 with concrete representative of Fukushima Daiichi Nuclear Plants [54].

- UO_2–ZrO_2 / SiO_2–CaO–Al_2O_3 system

Heat treatments on *corium*/concrete mixtures at well controlled temperatures were performed by Quaini et al. [53]. Two compositions were investigated with a mixture of UO_2 and ZrO_2 for *corium*, and two types of concrete: a limestone one (rich in CaO, corium 1 sample) and a siliceous one (rich in SiO_2, corium 2 sample). The samples were heated to 2500 K for 30 min and then quenched. The microstructures of the samples are shown in Fig. 8 (a) and (b) for corium 1 and corium 2 samples, respectively. As shown in Fig. 8, the calculations of the solidification paths are in good agreement with the experimental data:

For corium 1 enriched in CaO, a single liquid phase is predicted at 2500 K and the primary solid phase to form is the mixed oxide (U,Zr,Ca)O_2; the analysis showed the presence of $(Ca,Al,Zr)_3Si_2O_7$ and $(Ca,Zr,U)_2SiO_4$ phases that are predicted to form by the calculations although the solubility of Al and Zr in these phases is not yet modelled. For corium 2 enriched in SiO_2, two liquid phases are formed at 2500 K, in agreement with the calculations; the small size of the phase precipitates made it impossible to identify precisely the phases. Only SiO_2 was clearly identified.

The effect of the SiO_2/CaO composition of the concrete on the formed phases is well reproduced by our calculations.

- VULCANO corium concrete interaction test VF-U1

The VF-U1 test was performed to simulate the corium/concrete interaction (CCI) representative of Fukushima Daiichi 1F1 Nuclear Plants [54]. Prototype corium (12 Zr – 15.5 ZrO_2 – 59 UO_2 – 13.5 steel in w. %) was melted by induction heating and poured into a concrete (69.4 SiO_2 – 12.2 CaO – 12.3 Al_2O_3 – 6 Fe_2O_3 in w. %) section under air. The

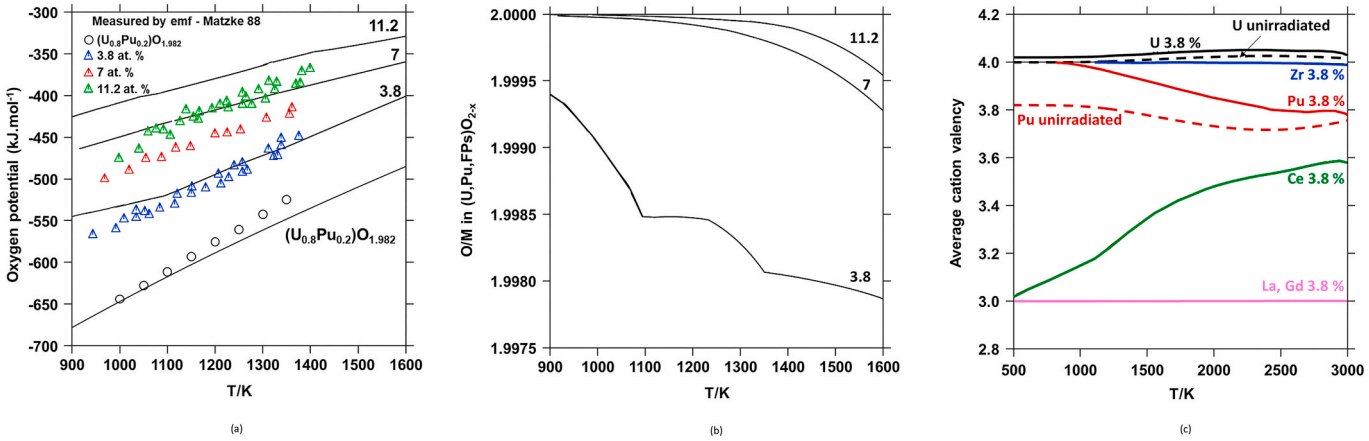

Fig. 11. (a) Calculated oxygen potential versus temperature for MOX fuels with burnups of 3.8, 7 and 11.2 % FIMA compared to the emf measurements by Matzke [55]; (b) Calculated oxygen to metal ratio versus temperature of the matrix $(U,Pu,FPs)O_{2-x}$ with FPs: Fission products; (c) Calculated average cation valency in the fluorite matrix versus temperature for unirradiated and 3.8 % FIMA burnup fuel.

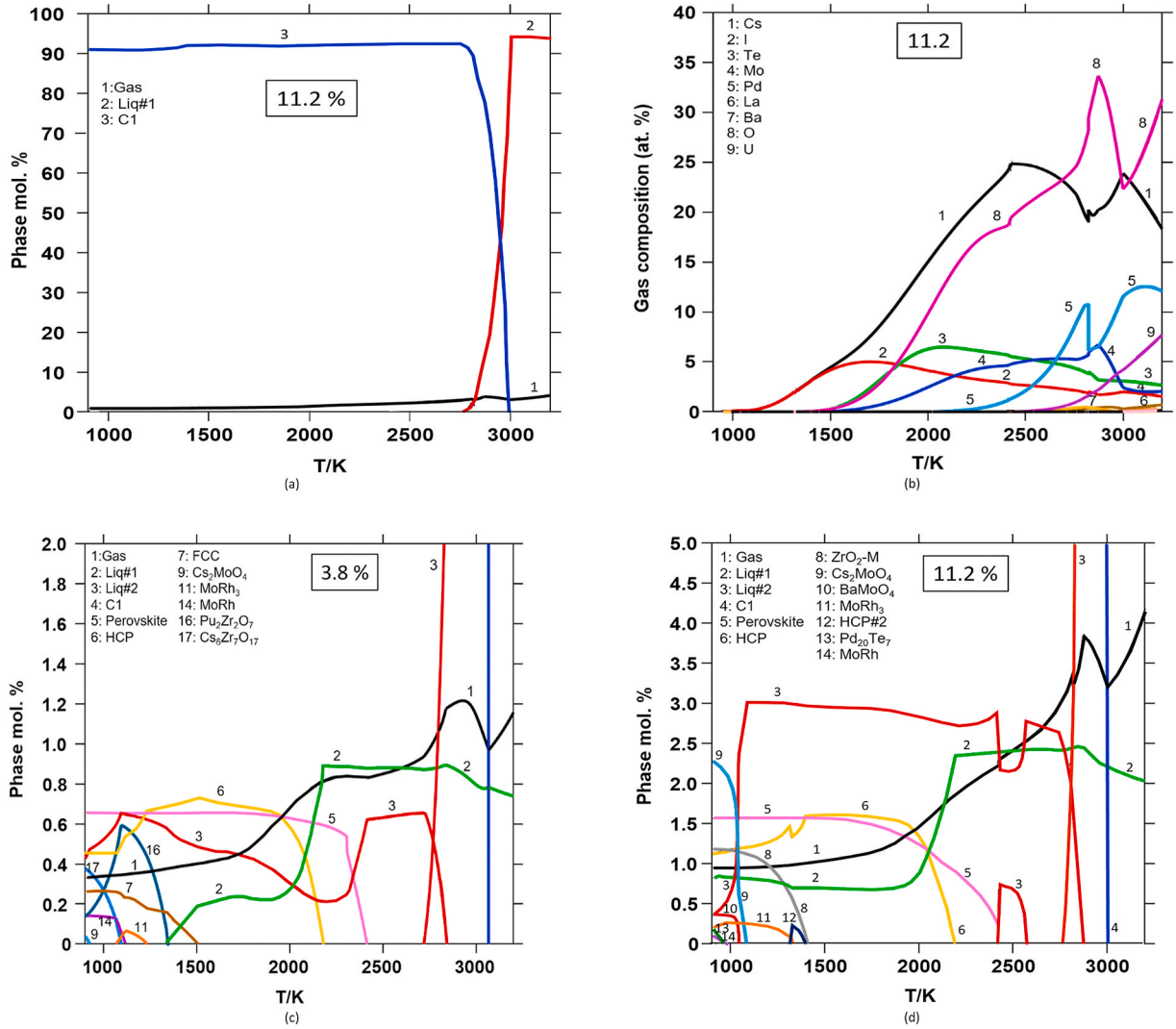

Fig. 12. Calculated (a) phase mole fraction for MOX fuel for the 11.2 % burnup as a function of temperature; (b) gas composition; (c) zoom showing the fission product phases for the 3.8 % burnup; (d) zoom showing the fission product phases for the 11.2 % burnup.

interaction occurred for 15 min with an initial temperature of about 2200 K. The microstructure of the solidified corium pool (sample 4 in Ref. [54]) is shown in Fig. 9. The microstructure is constituted of a silicon rich matrix, zirconium and uranium rich zones as well as iron rich regions.

Thermodynamic calculations were performed at 2190 K using the overall composition of sample 4 measured by Energy Dispersive Spectroscopy (EDS; given in Table 2 in Ref. [54]). At 2190 K, the phases predicted to form from the calculations are:

- 88.5 mol. % of an oxide liquid phase (liquid#1 with 64.3 O – 21.5 Si – 5.5 Al – 4.3 Ca – 2.6 U–1.8 Zr in at. %) containing the main components of the concrete (SiO_2–CaO–Al_2O_3) in which a small amount of uranium and zirconium is dissolved. The solidification path of this liquid phase is presented in Fig. 10.

According to the calculations, during cooling, zirconium and uranium are rejected from the liquid phase by forming various mixed oxides of uranium and zirconium, either cubic ($(Zr_{0.6}U_{0.35}Ca_{0.05})O_2$–C) at 1900 K and $(U_{0.91}Zr_{0.09})O_2$–C at 1800 K) or tetragonal ($(Zr_{0.83}U_{0.14}Ca_{0.03})O_2$-T at 2000 K and $(Zr_{0.83}U_{0.15}Al_{0.02})O_2$-T at 1800 K) with different Zr/U ratios and containing small amounts of aluminium and calcium. This is in very good agreement with the EDS and X-Ray Diffraction (XRD) analysis of this region of sample 4 in which tetragonal and cubic mixed oxides of uranium and zirconium containing small amounts of aluminium and calcium were found (called Corium elements Rich Nodules (CRN) in Ref. [54]). Moreover, the composition of the liquid at 1600 K (64 O – 23.4 Si – 6.5 Al – 5 Ca – 0.7 U–0.4 Zr in at. %) matches well with the measured composition of the amorphous matrix (average ~ 59 O – 26 Si – 5 Al – 4 Ca - 0.3 U–0.7 in at. %), called CEM (Concrete Elements rich Matrix) in Ref. [54]. We can conclude that during the CCI interaction, an oxide liquid phase containing the concrete components dissolved several percent of UO_2 and ZrO_2. During cooling, the mixed oxides have precipitated and the liquid phase has been quenched at about 1600 K. Also, the oxide phase found with the composition (65.1 O – 2.1 Al – 8.4 Si – 1.4 Ca – 17.7 Zr – 3.8 U in at. %) could correspond to the $(Zr,U)SiO_4$ phase predicted to form below ~1730 K in our calculations.

- 7.5 mol. % of $(Zr_{0.8}U_{0.15}Ca_{0.05})O_2$; this phase could correspond to the observed large size ZRO (Zirconium Rich Object) or CRN regions. In Ref. [54], these regions were found to be heterogeneous with a high zirconium rich oxide ($(Zr_{0.93}U_{0.07})O_2$) at the center whereby content decreases towards the edge, up to an average composition $(U_{0.5}Zr_{0.5})O_2$ having a two-phase microstructure containing a mixture of U and Zr rich mixed oxides and a small amount of minor elements (i.e., Si, Ca, Al, …). The calculations show that during cooling, the mixed oxide $(Zr_{0.8}U_{0.15}Ca_{0.05})O_2$ decomposes into several cubic and tetragonal mixed oxides with different Zr/U ratios, which could explain the presence of these oxide phases with different compositions. At 1400 K, 69 mol. % of $(Zr_{0.95}U_{0.03}Ca_{0.02})O_2$-T, 13 mol. % of $(U_{0.92}Ca_{0.06}Zr_{0.01})O_2$ and 18 mol. % of $(Zr_{0.74}Ca_{0.16}U_{0.10})O_{2-x}$ are predicted to form, which could correspond to CRN and ZRO zones in Ref. [54].

- 4 mol. % of a metallic liquid phase (liquid#2 with 36 Si – 28 Fe – 27 Cr – 9 Ni in at. %). This could correspond to the iron rich metallic droplets found in sample 4 in Ref. [54] whose exact composition is not given. The main components are Fe and Ni. Cr, S, P and Cu are found as minor elements. In Refs. [54], the authors mention that this alloy is made of martensite because the only phase detected by XRD is BCC. In the calculations, a large amount of silicon is found, which is in disagreement with the analysis. The phases that are predicted to form at 1300 K are: (Fe,Cr)Si, Cr_3Si and FCC (Ni,Fe,Cr) and BCC (Fe,Si,Cr,Ni) solid solutions.

These results show that during the corium/concrete interaction, two immiscible liquid phases form, the oxide liquid matrix containing the main concrete components and a small amount of uranium and zirconium, and the metallic liquid phase mainly constituted of the steel elements. The uranium and zirconium corium components are mainly located in the $(Zr,U)O_2$ mixed oxide large nodules in which a small amount of calcium and aluminium is dissolved. Calculations considering the solidification of each phase from 2190 K reproduces well the formed phases in the VF-U1 VULCANO test.

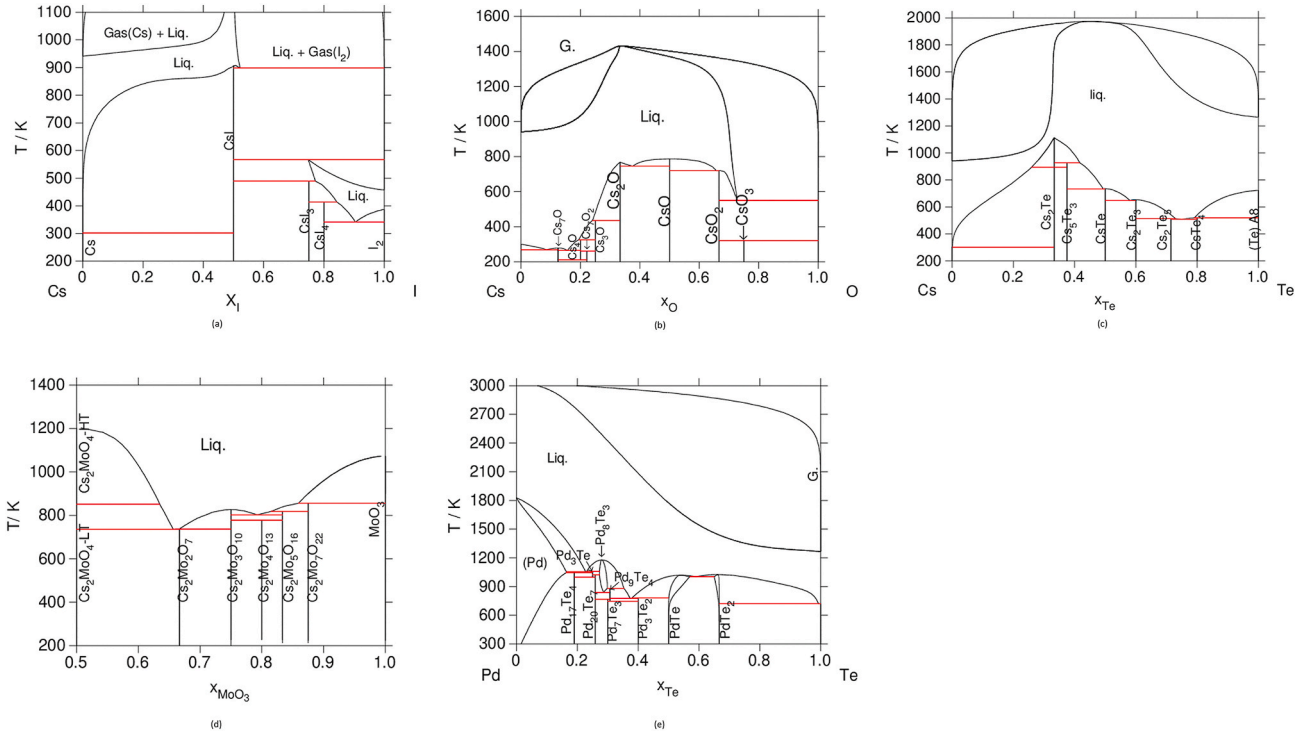

Fig. 13. Calculated phase diagrams of Cs–I (a). Cs–O [37] (b). Cs-Te [41] (c). Cs_2MoO_4–MoO_3 [12] (d) and Pd–Te [43] (e) systems with the TAF-ID database. The compositions are in atomic fraction.

5.2. Irradiated oxide MOX fuel chemistry

To illustrate the capabilities of the TAF-ID database, calculations on MOX fuels containing 20 % PuO_2 irradiated in the Phénix reactor with different burnups (fuel utilization) ranging from 3.8 to 11.2 % FIMA (Fissions per Initial Metal Atom: fraction of fuel atoms that underwent fission) are presented. This example was chosen because oxygen potential measurements by Matzke et al. [55] are available on these irradiated fuel samples as well as on the unirradiated oxide $(U_{0.8}Pu_{0.2})_{1.98}$ sample to study the effect of burnup.

For the thermodynamic calculations, the input data for the chemical compositions of the irradiated fuels at 3.8, 7 and 11.2 % FIMA are based on the elemental yields of fission products in a Phénix fuel pin calculated by the Darwin code [56–58] (Table 3).

5.2.1. Oxygen potential versus burnup

The oxygen potentials for the three irradiated fuels and for the unirradiated MOX $(U_{0.8}Pu_{0.2})_{1.98}$ are calculated in Fig. 11 (a) and compared to the experimental data measured by emf (electromotive force measurements) by Matzke et al. [55].

The calculated and experimental data for the unirradiated fuel $(U_{0.8}Pu_{0.2})O_{1.982}$ are in very good agreement, which validates the Calphad model on the U-Pu-O system [38]. A very good agreement is also obtained for the 3.8 % burnup. For higher burnups of 7 and 11.2 %, the calculated oxygen potential data are ~40 kJ/mol higher than the experimental values, corresponding to a relative deviation of about 9–10%. The present results show that the oxygen potential increases significantly with burnup in agreement with the literature data, because the fission products do not combine all the oxygen from the fission actinides [55,59].

The initial oxygen to metal ratio of the fuel is around 1.98. As shown in Fig. 11(b), the calculated oxygen stoichiometry of the fluorite matrix of the irradiated fuels increases with burnup up to values close to 2. The fluorite matrix remains slightly hypo-stoichiometric in oxygen with an oxygen to metal ratio close to 2 at low temperature that significantly decreases with increasing temperature up to ~1.99 for the three burnups at 2750 K. The oxygen potential is very sensitive to the initial oxygen to metal ratio. By taking 1.975 instead of 1.983 for the initial O/M ratio at 11.2% burnup, the agreement is very good with the experimental oxygen potential data. A slight decrease in the overall oxygen content of the fuel is a realistic assumption when considering the very high temperature level in the center of the pellet, which causes vaporization of uranium oxides in this region. Moreover, the large temperature gradient in the fuel pellet leads to the migration of many chemical elements along the pellet radius. One of the consequences is that the volatile fission products Cs, I, Te, Mo, Pd migrate into the rim of the fuel pellet to form a layer enriched in fission products called JOG. This phenomenon becomes more and more predominant with increasing burnup and affects the local fission product composition and thus the oxygen potential of the fuel. This could also explain the discrepancies for the 7 and 11.2 % burnups.

In Fig. 11(c), the average valencies of the cations in the fluorite matrix are calculated in both the unirradiated dioxide $(U_{0.8}Pu_{0.2})O_{1.982}$ and 3.8 % burnup fuel. In our model, the fluorite matrix is described by the following three sublattice model:

$(U^{3+},U^{4+},U^{5+},Pu^{3+},Pu^{4+},Zr^{4+},Zr^{2+},Ce^{3+},Ce^{4+},La^{3+},Gd^{3+})(O^{2-},Va)_2(O^{2-},Va)$

In $(U_{0.8}Pu_{0.2})O_{1.982}$, when the oxygen to metal ratio is lower than 2, at low temperature, the valencies of uranium and plutonium are 4 and 3.8, respectively. In the irradiated fuel, the lanthanides La and Gd are 3+, zirconium remains 4+, and cerium valency is 3+ at low temperatures and increases with temperature. To compensate these low valency states of the fission products, both uranium and plutonium are oxidized up to ~4.02 and 4, respectively, at low temperature. This increase in the U^{5+} and Pu^{4+} content explains the increase in the oxygen potential and oxygen stoichiometry of the fuel matrix with burnup.

In the following section, the chemistry of the other fission products is investigated.

5.2.2. Fission product phases and solid/liquid transitions

5.2.2.1. Phase equilibria in the 11.2 % FIMA irradiated fuel. In Fig. 12(a), the molar percentages of the major phases (the fluorite matrix denoted C1, the liquid and the gas phases) in the irradiated fuel with 11.2 % burnup are calculated as a function of temperature. The gas composition is given in Fig. 12(b). The fuel is mainly constituted of the fluorite matrix $(U,Pu,Ce,La,Gd,Zr)O_{2-x}$, where lanthanides and zirconium are dissolved. Small fractions of secondary phases are formed (Fig. 12(d)). For the solutions, the main constituting elements in the phases are indicated in parenthesis according to decreasing values of the concentrations. All the compositions are given in at. %.

From 900 to 1500 K, the fission products are located in the following phases:

- Cs_2MoO_4 which melts at 1100 K following a eutectic reaction (Cs_2MoO_4 + $BaMoO_4$, = LIQ#2), leading to the formation of the oxide liquid denoted LIQ#2 enriched in (Cs, O, I, Mo, Ba);
- The perovskite phase $BaZrO_3$, one of the main phases, that melts at 2416 K;
- The HCP metallic solution enriched in (Ru, Tc, Mo, Pd) whose composition varies significantly with temperature and is one of the main phases; its melting occurs at 2187 K;
- ZrO_2-m (monoclinic) which is stable up to 1400 K. Above this temperature, zirconium is dissolved in the fluorite matrix according to the UO_2–ZrO_2 phase diagram [45];
- The gas phase containing mainly CsI;
- A metallic liquid phase LIQ#1 enriched in (Pd, Te, Mo). The formation of this liquid at such low temperature can be explained by the existence of a low temperature eutectic in the Pd–Te system (Fig. 13);
- $BaMoO_4$, which is consistent with the work done by Muromura et al. [60] on SIMFUEL samples showing that for oxygen potential of around −300 kJ/mol at 1673 K, both perovskite and $BaMoO_4$ phases precipitate as secondary oxide phases;
- Small amounts of intermetallic compounds MoRh, $MoRh_3$ and $Pd_{20}Te_7$ which are progressively incorporated in the metallic HCP and LIQ#1 phases, respectively;

At higher temperatures (T > 1500 K).

- The irradiated fuel is constituted of the $(U,Pu,FP)O_{2-x}$ matrix with small fractions of oxide liquid LIQ#2, metallic HCP and perovskite oxide precipitates, and metallic liquid LIQ#1;
- The gas whose fraction increases with temperature incorporates more and more species (CsI, CsTe, Cs_2MoO_4, Cs, Te, Pd .). It causes the decrease in the Te and Cs contents in LIQ#1 and LIQ#2, respectively;
- Above 1800 K, the metallic liquid LIQ#1 fraction steeply increases due to the HCP metallic precipitates melting (at 2187 K);
- The perovskite phase $Ba(Zr,U,Mo)O_3$ incorporates a few percent of uranium and molybdenum up to its melting at 2416 K;
- At 2600 K, the stable secondary phases are: LIQ#2 (O, Mo, Ba, Cs, Pu), gas (Cs, Cs_2MoO_4, Te, Pd, CsI, CsTe, UO_3, BaO …), LIQ#1 (Ru, Pd, O, Rh, Mo, Tc, Pu);
- The fuel matrix starts to melt at 2743 K. The resulting oxide liquid fraction increases up to the liquidus temperature (2998 K).
- At 3000 K, the two immiscible liquids, metallic (Ru, Mo, O, Pd, Rh, Tc, Pu) LIQ#1 and oxide (O,U,Pu …) LIQ#2 are in equilibrium with the gas (Cs, Pd, UO_3, Te, CsI, Cs_2MoO_4, UO_2 …), which is quite common in metal-oxygen systems where miscibility gaps in the liquid state are often observed.

Table 4
Calculated solid/liquid temperature transitions in $(U_{0.8}Pu_{0.2})_{1.98}$ and irradiated fuels compared to the data from Hirosawa et al. [66]. The calculated O/M ratio of the fuel matrix is reported in parenthesis at both solidus and liquidus T. The calculations were performed either with all the phases (first case) or considering the fuel matrix alone (second case).

Fuel	Calc. incipient melting T of the fuel matrix (K) All phases	Calc. Liquidus T (K) All phases	Calc. Liquidus ($T_{(U_{0.8}Pu_{0.2})_{1.98}}$ - T irrad. fuel) (K) All phases	Exp. melting T Hirosawa [66] for 30% Pu (K)	Calc. solidus T of the fuel matrix alone (K)	Calc. Liquidus T of the fuel matrix alone (K)
$(U_{0.8}Pu_{0.2})_{1.98}$	3069 (1.982)	3107 (1.958)				
3.8%	2721 (1.99)	3069 (1.97)	38	3049 ± 35	3000	3079
7%	2754 (1.99)	3040 (1.98)	67	3027± 35	2975	3060
11.2%	2761 (1.99)	2998 (1.98)	109	3010 ± 35	2939	3034

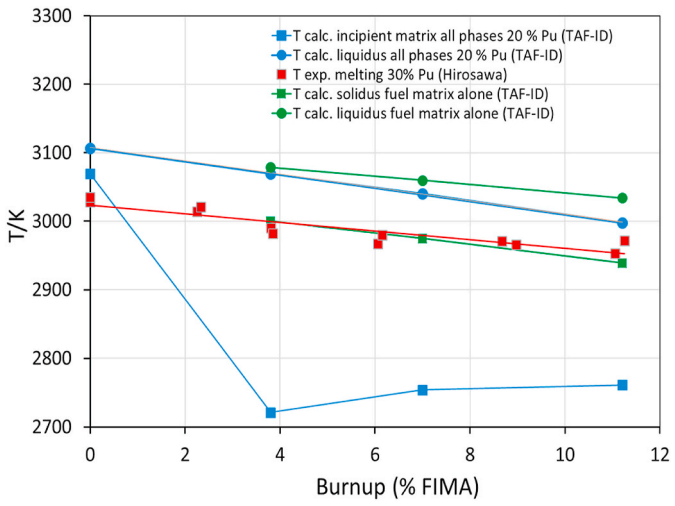

Fig. 14. Calculated incipient melting of the fuel matrix (blue square) and liquidus temperature (blue circle) for MOX fuel with 20 % Pu as a function of burnup with all phases. Calculated solidus (green square) ans liquidus temperatures (green circle) of the fuel matrix containing fission products alone. Comparison with the experimental data by Hirosawa et al. [66] on 30 % Pu MOX fuel (red square). (For interpretation of the references to color in this figure legend, the reader is referred to the Web version of this article.)

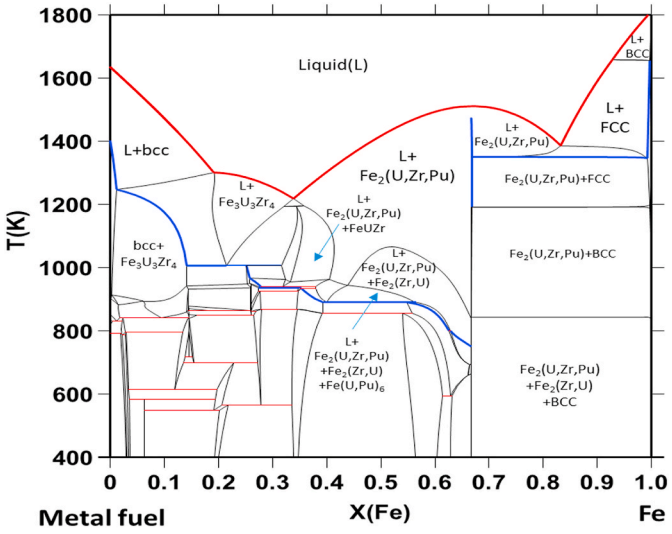

Fig. 15. Calculated phase diagram between a typical metal fuel (U-19 wt%Pu-10 wt%Zr) and iron Fe. The liquidus and solidus lines are marked in red and blue. Respectively. (For interpretation of the references to color in this figure legend, the reader is referred to the Web version of this article.)

The formation of small amounts of both metallic and oxide liquid phases at T < 1500 K can be explained by the low melting point of compounds containing cesium, iodine and tellurium as well as eutectic reactions existing in those systems as shown in Fig. 13.

Unfortunately, no results on the microstructural characterization of these irradiated MOX fuels were found. So a comparison with characterizations performed on other irradiated MOX fuels is performed.

The calculations can be compared with characterizations on similar irradiated MOX fuels using Scanning Electron Microscopy (SEM), Electron Probe Micro-Analysis (EPMA) and more recently Transmission Electron Microscopy (TEM) [61–63].

In the MOX fuel (initially containing 20 % Pu) irradiated in the POUSSIX experiment (burnup 9 % FIMA) [62], the following precipitates were observed:

- The HCP precipitates also called FMPs (Five Metal Particles), containing (Mo, Tc, Ru, Rh, Pd). The calculated composition in at. % at 2100 K (Mo 11.9 - Tc 11 - Ru 57.8 - Rh 10 - Pd 9.3) is in good agreement with the measurement (Mo 17.6 - Tc 13.2 - Ru 58 - Rh 4.8 - Pd 6.4);
- The perovskite precipitates $(Ba,Cs)(U,Zr,Pu)O_3$ which vary in composition of Cs, U and Pu depending on the location in the fuel. The formation of the ceramic phase $Ba(Zr,U)O_3$ is predicted by our calculations. A good agreement is found although the calculations underestimate the U content (exp.: 6.9/calc.: 2.6 at. % at 2100 K, ~5 at. % at 2400 K). Larger discrepancies are found when cesium and plutonium are dissolved in the precipitates because the solubility of cesium and plutonium is not yet modelled in our database;
- Ceramic phases containing (Ba 3.8 – Cs 6.6 – U 3.5 - Mo 12.5 – Te 9.0 – O 63 at. %). This composition is not far from the LIQ#2 one calculated at 2100 K: (Ba 5.9 – Cs 17.4 – Mo 15.1 – O 61), which corresponds to a mixture of (Cs_2MoO_4 + $BaMoO_4$ + MoO_3) species.

In POUSSIX, a fuel/steel cladding interaction occurred leading to the formation of a steel-Mo-Pd rich layer. This is consistent with the high volatility of Pd above 1600 K found in our calculations (Fig. 12(b)). It can be assumed that palladium migrated towards the rim zone of the fuel and interacted with the cladding forming Fe–Pd phases (observed in POUSSIX). Also, the fuel gap was filled with Cs–Ba–Mo oxitelluride and Cs uranate phases, whose composition is close to the one of LIQ#2 in our calculations. The presence of these phases could be explained by the migration of gas, LIQ#1 (Pd,Te) and LIQ#2 (Cs,Mo,I,Ba,Mo) phases towards the fuel gap.

In the MOX fuel containing 30 % Pu irradiated at 13.7 % FIMA, Parrish et al. [61] observed the following secondary phases:

- The HCP metallic FMPs precipitates (Mo 6.4 - Tc 13.8 - Ru 57 - Rh 17.1 - Pd 3.8 at. %); the calculated composition at 1500 K (Mo 17.8 – Tc 11.2 – Ru 49.5 – Rh 13 – Pd 8.5 at. %) is in overall good agreement although the measured Mo content is much lower;

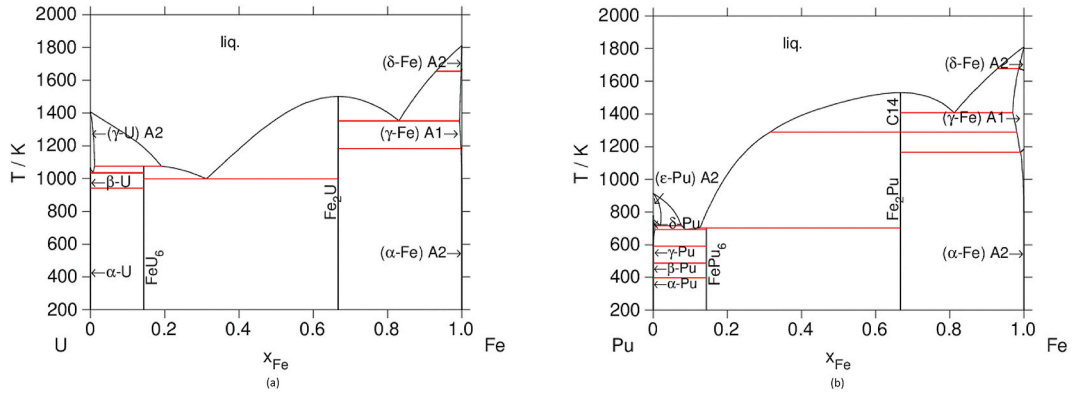

Fig. 16. Calculated phase diagrams of Fe–U (a) and Fe–Pu (b) systems using the TAF-ID database [12]. The compositions are in atomic fraction.

- Pd-rich precipitates (Pd 70–25.5 Te – 5 U at. %) found in the cooler region at the rim of the pellet. These precipitates could correspond to the liquid phase LIQ#1 (Pd 68 – Te 17.4 – Mo 8.4 – Tc 3.1 – Ru 2.6 at. %) in our calculations. And as suggested by the authors, the migration of the volatile fission products in the gas and liquid phase could lead to the formation of Pd–Te rich phases in the fuel/cladding gap;
- Small perovskite precipitates whose composition could not be analyzed.

Less numerous secondary phases were observed by Parrish. This could be due to a relatively low centerline temperature of 1500 K compared to a more typical value of 2200 K.

It can be concluded that even if the present calculations were performed using the overall fuel composition, which does not take into account the mass transport of the elements within the fuel pellet, the main phases are well predicted by the calculations.

Moreover the migration of the small fractions of metallic and oxide liquid phases predicted by our calculations could explain the composition of the fission products enriched zones (JOG) that are observed in the fuel/gap region. This can be achieved thanks to the full modelling of the solid and liquid solutions in the TAF-ID database.

In a recent work by Samuelson et al. [64], calculations have been performed with the TAF-ID database on the NESTOR3 irradiated fuel taking into account the local composition of the fission products along the pellet radius. An overall good agreement with the characterizations was obtained. Recently, a coupling of the TAF-ID and the Open Calphad code with the GERMINAL Fuel Performance Code has been performed, which allows taking into account the element mass transport (section 5.4.4) [65]. It is expected that this detailed modelling will improve the prediction of the thickness of this FP enriched layer (JOG), which affects the fuel thermal conductivity and therefore the temperature distribution in the fuel pellet [65]. Also, preliminary calculations with the TAF-ID on the corrosion of the cladding by these fission products is ongoing in GERMINAL to further predict the life time of the cladding materials in Sodium Cooled Fast Reactors (SFR).

5.2.2.2. Influence of the burnup on the fission product phases. The fractions of the secondary phases in the 3.8 % FIMA irradiated fuel are calculated in Fig. 12(b) and can be compared to the results for the 11.2 % FIMA in Fig. 12(c). As expected, the total fraction of secondary phases is lower for a decreasing burnup.

At low temperature (T < 1500 K), the phases at 3.8 % burnup are.

- The perovskite $BaZrO_3$, which melts at 2414 K;
- The LIQ#2 phase containing (Cs, O, Te, Mo, I), which is a mixture of (Cs_2Te + Cs_2MoO_4 + CsI);
- The HCP phase enriched in (Ru, Mo, Tc, Pd), which melts at 2180 K;
- The gas phase;

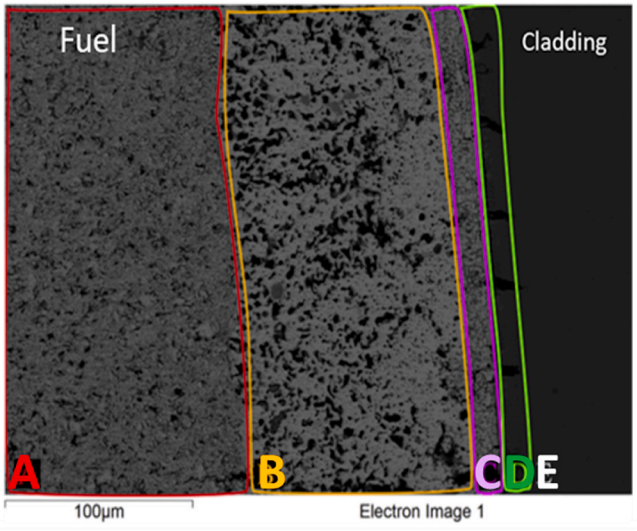

- **Zone A.** U matrix with Ru-U, Mo-U, and lanthanides precipitates.
- **Zone B.** containing Fe (1-2 wt. %) and Ni:
  - Fe, Mo, and Ru rich separate layers
  - Zr precipitates.
- **Zone C.** containing up to 5 wt. % Fe but no Ni.
  - Pd-Rh-Ce-Nd-Zr association
  - Ce+Nd, Mo, and Zr rich precipitates
- **Zone D.** Ni depleted region in the cladding.
- **Zone E.** Cladding (68 Fe – 18 Cr – 14 Ni wt. %).

Fig. 17. Reaction zone at the U-5Fs fuel/cladding interface [69].

- The FCC phase with (Pd, Mo, Tc, Ru), which melts at 1500 K leading to the formation of the metallic liquid phase LIQ#1 enriched in (Pd, Cs, Mo, Te, Ru, Tc, Rh);
- $Cs_6Zr_7O_{17}$, $Pu_2Zr_2O_7$ oxides and MoRh compounds.

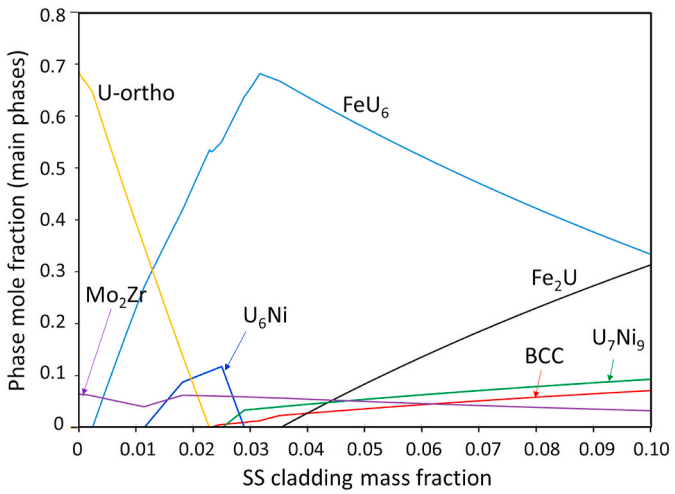

Fig. 18. Calculated mole fraction of the major phases which form during the interaction between the U-5Fs fuel and stainless steel.

At this lower burnup, $BaMoO_4$ is not predicted to form, which is consistent with the lower oxygen potential (see Muromura et al. [60]). The main oxide phase is the perovskite. Also, the fraction of Cs_2MoO_4 is negligible. Consequently, the LIQ#2 relative fraction is lower than for the 11.2 % FIMA burnup. Furthermore, $Cs_6Zr_7O_{17}$ and $Pu_2Zr_2O_7$ oxides form instead of ZrO_2-m probably due to the lower oxygen potential. At high temperature, zirconium is dissolved in the fluorite matrix.

Concerning the metallic phases, there is no metallic LIQ#1 phase below ~1300 K. Instead, the FCC phase is stable together with the HCP phase which is consistent with the work of Muromura et al. [60].

Kleykamp et al. [63] studied the composition and structure of metallic (HCP, BCC and FCC) and perovskite phases as a function of initial O/M ratio and burnup of irradiated oxide fuels. The molybdenum content of the metallic phases strongly depends on the local oxygen potential of the fuel, which is fixed by its initial O/M ratio and burnup. The higher the oxygen potential (and the O/M ratio), the lower is the molybdenum fraction in the HCP phase. This is in agreement with our calculations at 1973 K in which the Mo content in the HCP phase is of 24.3 at. % for 3.8 % FIMA and 14.2 at. % for 11.2 % FIMA. Also, according to Kleykamp et al. [63], both HCP and FCC phases are stable at high burnup, which is consistent with our results for 3.8 % FIMA. For 11.2 % FIMA, no FCC was found but instead a metallic liquid phase having the same composition was predicted to form, which may precipitate the FCC phase on cooling.

5.2.2.3. Influence of burnup on the melting temperature. The margin to melting of the fuel must be well predicted for safety related studies and to model the fuel thermal conductivity.

In a first step, the calculations on irradiated fuels were performed with all the phases, as in Fig. 12. As small amounts of liquid phases form at low temperature, the incipient melting temperature of the fuel matrix is reported instead of the solidus temperature. It corresponds to the temperature at which the matrix $(U,Pu,FP)O_2$ starts to melt.

The calculated incipient melting and liquidus temperature data for $(U_{0.8}Pu_{0.2})O_{1.982}$ and for the three irradiated fuels are reported in Table 4 and plotted in Fig. 14. The calculated temperatures are compared with the experimental data of Hirosawa et al. [66], based on measurements on irradiated fuels (with 28–30 wt % Pu) using the thermal arrest method.

The calculated liquidus temperatures of irradiated fuels are lower than for unirradiated $(U_{0.8}Pu_{0.2})_{1.98}$ oxide and decrease with burnup. A linear dependence with burnup is found as for the melting temperature measurements by Hirosawa et al. [66]. In their work, Hirosawa et al. [66] report a single melting temperature that corresponds to the solidus temperature in their measurements. The calculated incipient melting temperatures for the irradiated fuel matrix are in disagreement with these experimental data leading to much lower values (~2720–2760 K), which do not vary significantly with burnup. These discrepancies may be due to the existence of eutectic reactions between the fuel matrix (U, Pu,FP)O_2 and secondary fission product phases.

To check this assumption, in a second step, the solidus and liquidus temperatures of the fuel matrix (U,Pu,FP)O_2 alone (with its composition at 2700 K) were calculated (in green in Fig. 14). In that case, the solidus temperatures compare very well with the experimental data for irradiated fuels with 30 % Pu. The liquidus temperatures are slightly higher than in the first case where we considered all the phases. Consideration of only the fuel matrix in the calculations is supported by the fact that the fraction and size of the secondary phases are very low. Thus, the possible reaction between the fuel matrix and these small precipitates may be a local phenomenon, which may not be detected in a thermal arrest test. It shows that to estimate the margin to melting of the irradiated MOX fuels, the calculations have to be performed considering the fuel matrix containing the dissolved fission products alone. The solidus and liquidus temperatures of irradiated MOX fuels decrease with the concentration of dissolved fission products, which increase with burnup. More systematic calculations could be performed with the TAF-ID as a function of Pu content and burnup. Also, more measurements on irradiated samples would be very useful to continue this comparison and conclude on the validation of our calculations.

The present calculations on irradiated MOX fuels show the value of the TAF-ID database, which allows to predict all the thermodynamic

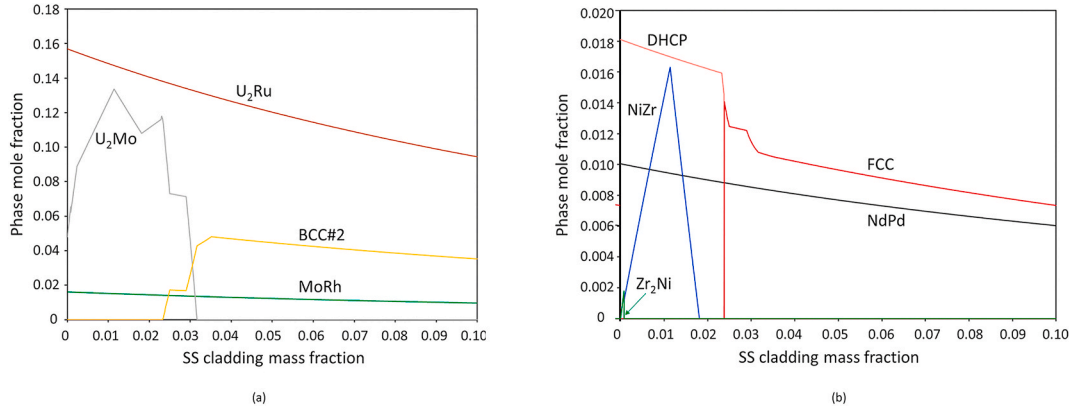

Fig. 19. Calculated mole fraction of the minor phases which form during the interaction between the U-5Fs fuel and stainless steel containing (a) Mo, Ru, Rh (b) Ce, Nd, Zr, Pd.

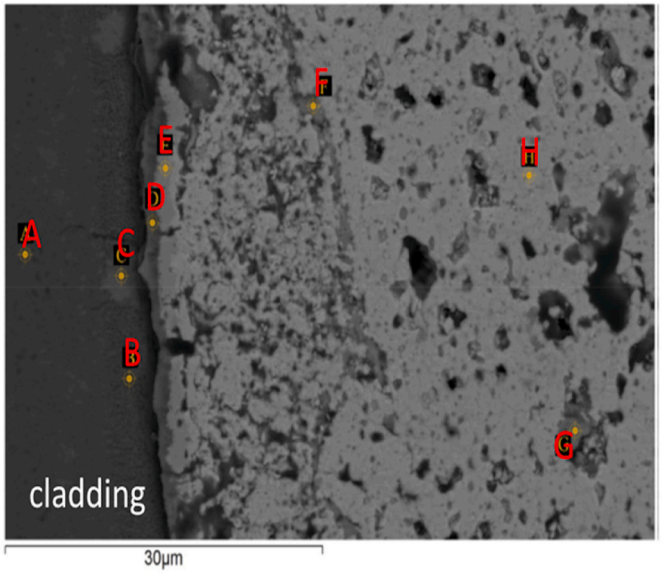

	Concentration (at%)									
POINT	Si	Cr	Fe	Ni	Zr	Rh	Pd	Ce	Nd	U
A		23.4%	75.8%	0.8%						
B		31.0%	69.0%	0.0%						
C	8.7%	28.2%	57.1%	4.0%				1.0%	1.0%	
D	3.9%	66.1%	15.3%	9.7%						4.9%
E		15.3%	42.6%	4.2%						37.9%
F				8.8%	29.6%	8.8%	8.8%	5.2%	15.1%	23.6%
G	4.2%			4.7%	74.7%				4.0%	12.3%
H			9.5%							90.5%

Fig. 20. Micrograph showing where the EDS analyse were performed [69]. A comparison with the calculations is presented.

- **Point H**, acquired in an area of the fuel with a low content of Fe is in good agreement with FeU_6 predicted by the calculations;
- **Point G**, a Zr rich precipitate containing Ni, U, and Si. Though Si was not considered in the calculations, the TAF-ID predicts a minor phase consisting of Zr_2Ni. The U content observed experimentally could be an influence of the surrounding U matrix;
- **Point F**, measured in a region where different precipitates were observed. The experimental composition could correspond to a mixture of the minor phases predicted by the TAF-ID: Ce–Nd, NiZr, NdPd, and the surrounding matrix. As indicated in Ref. [69], the Ce–Nd and NdPd phases were observed separately in this sample.
- **Point E**, acquired on a region of the fuel adjacent to the cladding. The measured composition could correspond to $(Fe,Cr,Ni)_2U$ in agreement with the Fe_2U phase predicted by the TAF-ID.

data (oxygen potential, vapor partial pressures …), the chemical composition of the fuel matrix and secondary phases, and temperatures of phase transitions for oxide fuels with different burnups under normal and off-normal conditions. The good agreement with the available experimental data shows the high degree of maturity of the database. But more experimental measurements would be helpful to continue this validation procedure.

5.3. Metallic fuels

5.3.1. (U-Pu-Zr) fuel/Fe interaction

An important factor for designing a metal fuel for fast reactors is the chemical interaction between the metal fuel and Stainless Steel (SS) cladding, FCCI. For the design under normal operation and transient conditions, the identification of the eutectic liquefaction temperature

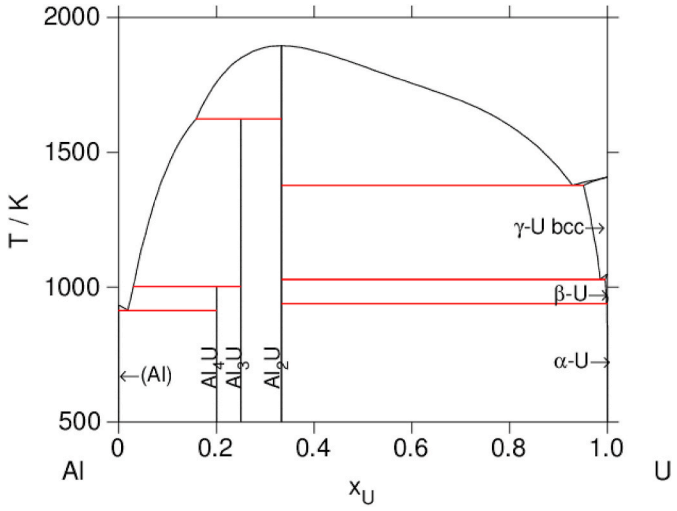

Fig. 21. The uranium-aluminium phase diagram is shown as computed from the TAF-ID [12,75]. The compositions are in atomic fraction.

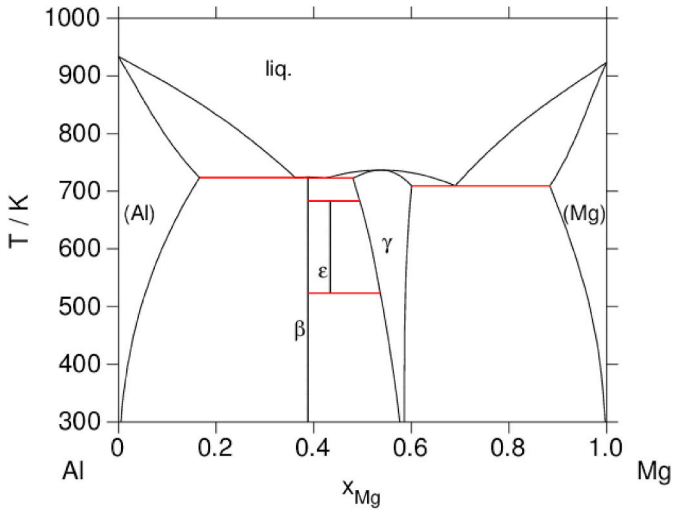

Fig. 22. The aluminium-magnesium phase diagram is shown as calcualted by the TAF-ID [12,77,78]. The compositions are in atomic fraction.

and phase relations around the eutectic between the metal fuel and the SS cladding is indispensable. As an application, the phase diagram between a typical metallic fuel (U-19 wt % Pu-10 wt % Zr) and iron as a representative of the SS is plotted in Fig. 15. This type of diagram allows the prediction of the lowest temperature for liquid formation as a function of the quantity of iron that would react with the metal fuel. The lowest temperature is calculated at 751 K for about 66 mol. % of Fe. This very low value is due to the existence of very low eutectic reactions in both Fe–Pu (700 K: Liq = Fe_2Pu + $FePu_6$) and Fe–U (1000 K: Liq = Fe_2U + FeU_6) (Fig. 16). This suggests that a limited amount of Pu-rich liquid might be partially formed in a part of the diffusion path between the metal fuel and the SS in high burnup conditions.

The same calculation considering the SS cladding (Fe-12 wt % Ni-17 wt % Cr) instead of pure iron Fe leads to 730 K for the lowest temperature for liquid formation for 39 % mol. stainless steel (here, the Ni–Pu binary system is not yet modelled). An important factor is the solid/liquid ratio in the expected diffusion path between the metal fuel and the SS cladding. Hence, the detailed understanding for the liquid amount in solid/liquid mixture regions of these phase diagram will be very useful for improving the metal fuel design.

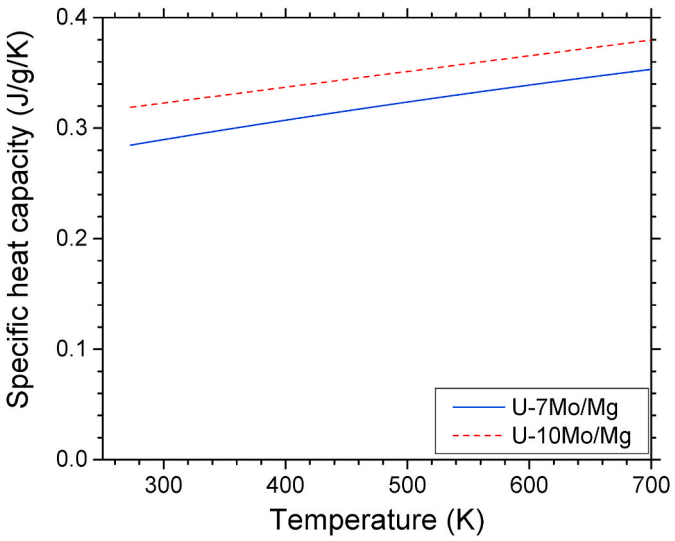

Fig. 23. Calculated specific heat capacity of U–Mo/Mg using the TAF-ID.

5.3.1.1. U-5Fs/steel cladding interaction. Fuel Cladding Chemical Interaction (FCCI) in an irradiated U-5Fissium (U-5Fs) sample is investigated. The U-5Fs fuel, which mimics the composition of the fuel used in the experimental Breeder Reactor II (EBR-II) [67,68], consists of uranium alloyed with 6 elements (i.e., Mo, Ru, Rh, Pd, Zr, and Nb here neglected) in a stainless steel 316 cladding [69]. After irradiation, one of these fuel elements was thoroughly characterised by SEM-EDS, with an emphasis on FCCI. The pre- and post-irradiation composition and dimensions of the sample, along with characterization results are available in Ref. [69]. Five major zones of chemical interaction were identified in the fuel/cladding interface which main characteristics are summarized in Fig. 17. There is a reaction zone (C + B) of ~150 μm thickness in which a few percent of Fe and Ni have diffused.

Thermodynamic calculations with the TAF-ID database have been performed on the U-5Fs sample at 813 K. The phases which form during the interaction with an increasing amount of Stainless Steel are calculated in Fig. 18 (for the main phases) and in Fig. 19 (for the minor phases with (a) Mo, Ru, Rh and (b) Ce, Nd and Zr).

The unaffected fuel by the reaction with the cladding is constituted of a matrix of uranium (orthorhombic) with a small fraction of U_2Ru, U_2Mo, Mo_2Zr, MoRh, NdPd compounds and (Ce,Nd) DHCP solution precipitates.

During the interaction with the stainless steel, the main phases predicted to form are: FeU_6, Fe_2U, U_7Ni_9, U_6Ni, $(Fe,Mo,Cr)_2Zr$. Also small fractions of additional BCC#2 (Mo,Nd,Cr) solution, NiZr, Zr_2Ni and FCC (Ce,Nd) solution are also calculated from the interaction with (Cr and Ni) from the cladding.

These results from the calculations are compared to two sets of experimental results: Fe and Ni X-ray maps, and semi-quantitative EDS analyses [69].

From the Fe and Ni X-ray maps, Harp et al. identified a rich Fe layer located right next to the cladding on the fuel side (zone C in Fig. 17) and a Fe–U interaction region (zone B indicated in Fig. 17), that extends for more than 100 μm into the fuel. According to calculations, these two layers could correspond to Fe_2U and FeU_6, respectively. Further support to this conclusion is presented in the semi-quantitative EDS/calculations comparison, below. As for Ni, the corresponding X-ray map presents a Ni-depleted region in the cladding, a rich Ni phase at the fuel/cladding interface, and an homogeneous distribution of Ni further into the fuel. TAF-ID calculations predict two main U–Ni phases: a Ni-rich phase with composition U_7Ni_9, which could correspond to the Ni rich layer next to the cladding, and a U rich phase, U_6Ni, which could be the region where Ni is homogeneously distributed in the fuel.

Semi-quantitative EDS analyses done on the same region where the X-ray maps were acquired, are summarized in Fig. 20 also adapted from Ref. [69].

In conclusion, and considering that EDS composition analyses are semi-quantitative, the phases predicted by the calculations with the TAF-ID in the region in interaction with the SS cladding are in qualitative good agreement with the experimental observations. It constitutes a first step to support the interpretation of the interaction in which kinetics must play a role. More accurate measurements would be useful to go further in the comparison. Also a deep experimental investigation of the phase diagrams of these systems is required to improve the models in the TAF-ID only based on the description of the binary sub-systems.

5.4. Thermodynamic data as a basis for thermal physical and kinetic properties and for coupling to multi-physics codes

The coupling of thermodynamic models to other physical models (diffusion, mass transport, thermal diffusion, thermalhydraulics …) is a promising approach to develop multi-physic computational tools to get a more realistic prediction of the high temperature behaviour of nuclear materials. A few examples are presented in this section.

5.4.1. Thermal conductivity of U–Mo fuels

Unlike power reactors, the objective of a research and test reactor is generally not to produce a large amount of heat, but rather to provide a neutron source that may be used for neutron diffraction experiments, isotope production or other material irradiations. One particular fuel design that has experienced significant research and development is uranium-molybdenum (U–Mo), which is often dispersed in a host matrix of aluminium (Al) or magnesium (Mg). In both designs, the fuel is clad in Al. These two particular designs are currently being investigated as Low Enriched Uranium (LEU) replacements for previous designs that employed Highly Enriched Uranium (HEU) to address non-proliferation concerns [70-72].

The survivability of U–Mo/Al and U–Mo/Mg fuels is strongly dependent on changes to their microstructure as a result of any phase transitions that may occur at elevated temperatures and the effects of irradiation. For instance, the inter-diffusion of atoms between U–Mo kernels and the bulk Al matrix in U–Mo/Al fuel results in the formation of an interaction layer which is primarily UAl_3 [73]. The stability of this phase is illustrated in the U–Al phase diagram shown in Fig. 21. The formation of this interaction layer has two detrimental effects on fuel performance: 1) it reduces the bulk thermal conductivity thereby increasing the maximum temperature; and 2) the thermal expansion coefficient is quite different from the bulk fuel material resulting in excessive swelling. Post-irradiation examination of irradiated U–Mo/Al fuel has determined that the two foregoing factors have contributed to failures of U–Mo/Al fuel [74].

As an alternative design to U–Mo/Al fuel, U–Mo/Mg fuel is being investigated at the Canadian Nuclear Laboratories for use as a driver fuel in research and test reactors. The primary impetus of replacing Al with Mg as the host matrix is because Mg is immiscible with U and Mo.

While neither U nor Mo readily react with Mg within the bulk fuel material, Mg does however react with Al, which is the primary alloying element of the cladding. Several intermetallic phases may form, which are illustrated in the Al–Mg phase diagram in Fig. 22. Neutron diffraction measurements by Xiao and Wang [76] have confirmed the formation of beta and gamma intermetallic phases between the U–Mo/Mg fuel and Al-cladding; however, the formation of these phases have not resulted in fracture of the fuel and cladding materials in laboratory tests [76].

Thermodynamic calculations have assisted thermal diffusivity measurements of U–Mo/Mg fuel using a Laser Flash Analysis (LFA) technique [79]. While the LFA method provides thermal diffusivity data, thermal conductivity is a more valuable parameter to be used in heat transfer calculations. Therefore, one must have a relationship for both

density and the specific heat capacity at constant pressure in order to convert thermal diffusivity to thermal conductivity. Thermodynamic calculations with TAF-ID were made on U–Mo/Mg fuel based on the constituent phase compositions measured via neutron diffraction to compute the thermal conductivity of the fuel [79]. This overall effort helped support safety analyses of U–Mo/Mg fuel irradiations at CNL.

Specific heat capacity values of U–Mo/Mg was computed for two different compositions using the TAF-ID (Fig. 23). This was used to compute thermal conductivity from thermal diffusivity measurements, which were ultimately used for in-reactor safety analyses [79].

5.4.2. Diffusion properties of UO_2 and MOX fuels

The DICTRA code is a computational code that couples a Calphad type thermodynamic database to a mobility database, allowing the modelling of diffusion data for multi-component materials as well as simulation of phase transitions controlled by diffusion. As an example, the thermodynamic model on the (U,Pu)$O_{2\pm x}$ mixed oxide [12,38] was coupled to a mobility database for oxygen [80,81]. With such coupled thermochemistry-kinetic model, it is then possible to calculate all diffusion data (self and chemical diffusion coefficients) for oxygen in the (U,Pu)$O_{2\pm x}$ mixed oxide for any Pu content, oxygen stoichiometry and temperature. The advantage of this approach is also that both thermodynamic and diffusion properties are linked by a simple point defect model (oxygen vacancy and interstitial). This computational tool can then be used to perform one dimensional simulations, as for instance, of a diffusion couple experiment or of the oxygen stoichiometry change during heat treatments [80,81]. The development of the mobility database for plutonium and uranium is ongoing. Thus, a full thermo-kinetic model on (U,Pu)$O_{2\pm x}$ mixed oxide will be soon available. The calculated diffusion data could be used for the optimization of the experimental conditions during MOX sintering and as input data for the mass transport models in fuel performance codes.

5.4.3. Coupling thermodynamics with phase-field

Phase-field models, typically applied to interfacial energy driven phenomena offer ready integration with Calphad free energies through their derivations [82,83]. This integration extends the range of applicability of the thermodynamic potential which generally correspond to bulk equilibrium, to nanoscale objects which are perturbed from the bulk equilibrium by interfacial effects or local heterogeneity. Additionally, they provide a ready link between chemical potential driven mass transport as described above with a phase change, such as diffusion-controlled interlayer growth between UMo/Mg fuel with Al cladding. The free energy of the system may be written in terms of the local state variables, e.g.: the concentration of species *i*, c_i, and the local phase, φ^{α}:

$$A = \int_V a(c_i, \varphi^{\alpha}) + a_{\sigma}(\varphi^{\alpha}, \nabla\varphi^{\beta}) \tag{12}$$

where $a(c_i, \varphi^{\alpha})$ is the composite Helmholtz free energy density, and $a_{\sigma}(\varphi^{\alpha}, \nabla\varphi^{\beta})$ is a function which includes interfacial energies and controls the interface width [80]. The composite free energy density is formed from the weighted sum of the pure phase *grand potentials*, which avoids implicit interfacial energy contributions [84].

This model was applied to interdiffusion of the fuel meat – Al cladding interface in U–Mo/Mg fuels, to capture the growth of the intermetallic layers. The thermodynamic properties from the TAF-ID database were used. The stoichiometric Al_3Mg_2 phase was approximated for computational purposes [85]. The composite function corresponds to the coexistence of Al-FCC and Al_3Mg_2. The system evolves to minimize the total free energy through interdiffusion of Al and Mg driven by gradients in their chemical potentials, and growth of the intermetallic layers according to the composite free energy surface.

5.4.4. Coupling thermodynamics with fuel performance codes

5.4.4.1. BISON.

Progress has been made in coupling parts of the TAF-ID database with the nuclear fuel performance code BISON [86]. The THERMOCHIMICA software [87] was used to compute thermodynamic equilibria. The overall intent of this coupling was to enhance predictive capabilities of oxygen transport, whereby the oxygen to metal ratio, O/M, of the fuel affects a number of material properties. In order to calculate correctly oxygen transport, one must work with gradients of the oxygen chemical potential, rather than oxygen concentration gradients. This becomes complicated for irradiated fuel, whereby the changes with fission and activation product concentrations with space and time coupled with a sharp temperature gradient have a significant effect on the oxygen potential.

Initial progress was focused on hyperstoichiometric UO_{2+x} fresh fuel to simulate heat transfer and oxygen transport. The coupled thermo-diffusion mass flux of component *k* is solved in this work in terms of the Onsager coefficients as [88]:

$$J_k = -L_{kk}\left[T\nabla\left(\frac{\mu_k}{T}\right) + Q_k^{*}\frac{\nabla T}{T}\right] \tag{13}$$

where L_{kk} are the proportionality coefficients, T temperature, μ_k is the chemical potential of component *k*, Q_k is the heat of transport. Here, the chemical potential of oxygen is computed directly by THERMOCHIMICA using the TAF-ID treatment for UO_{2+x} and is used in the above equation. With such a tool, the oxygen potential in a three-dimensional fuel pellet has been predicted [88].

Since the full thermodynamic calculation of the UO_{2+x} phase from TAF-ID is computed, a number of other useful parameters are computed internally, such as the site fraction of interstitial oxygen atoms and vacancies. These values are likely to be used in continued modelling efforts as input to material models. Future efforts will likely expand this work to include irradiated fuel from the TAF-ID and the effects of irradiation on fuel performance.

5.4.4.2. GERMINAL.

As mentioned in section 5.2, the TAF-ID database is used in the GERMINAL V2 Fuel Performance Code by coupling with the Open Calphad software [10] to evaluate the chemical state of (U,Pu)O_2 fuel and fission products in Sodium cooled Fast Reactors [65]. A mass transport model allows taking into account the migration of the most volatile fission products Cs, I, Te, Mo, Pd (with O) whose quantities are calculated with the TAF-ID, to estimate the JOG thickness as a function of burnup. For the first time, the coupling of a full Calphad modelling with a Fuel Performance Code was achieved which is promising for the improvement of the models on the fuel thermal conductivity and on the cladding attack by the fission products. Also, diffusion properties as presented in section 5.4.2 are planned to be taken into account.

6. Conclusion

In this paper, the TAF-ID thermodynamic database developed in framework of the OECD/NEA TAF-ID joint project is described. It contains the most relevant chemical systems of interest for oxide and metallic fuels and structural materials for Generation 2, 3 and 4 reactors. The use of a full Calphad modelling was adopted allowing calculations in both normal, abnormal and severe accident conditions. A few examples of key modelled systems are first given. Then, a few examples of application calculations are presented with a comparison to experimental data. For severe accident in LWRs reactors, metallic and oxide liquid phases compositions are calculated for in-vessel *corium* which is of upmost importance to predict stratification phenomena in the lower head of the reactor vessel during severe accident. Another example shows the capability of the TAF-ID database to calculate the solidification path for ex-vessel *corium* liquid compositions forming from the interaction between the in-vessel *corium* and the concrete basement.

Calculations are performed to interpret the microstructure of samples obtained during the VULCANO VF-U1 test. During the project, a big effort has been put on the modelling of fission product systems. The capability of the TAF-ID database to describe irradiated MOX fuels for fast breeder reactors is demonstrated by calculations of oxygen potential data and fission product phases that form with different burnups. In all these calculations, the agreement between calculated and experimental data is very good. Also, a complete description of the gaseous phase for these complex fuels allows calculating vapor pressure data that are essential for the fission product release and for the estimation of the source term during a severe accident. Other calculations are performed for metallic (U,Pu,Zr) fuel and U alloys containing fission products and their interaction with the steel cladding. Finally a few examples on how to use the TAF-ID database to provide input thermodynamic data for multi-physics modelling are given: the evaluation of thermal conductivity of U–Mo/Mg fuels, the development of a thermo-kinetic full modelling of the $(U,Pu)O_2$ fuel with the DICTRA software, a phase-field simulation on the U–Mo/Mg system, the incorporation of the UO_{2+x} thermodynamic model in the Bison Fuel Performance code and the evaluation of irradiated MOX fuel chemistry for SFR by coupling the Fuel Performance Code GERMINAL with the TAF-ID using Open Calphad. The second phase of the TAF-ID project is ongoing. The database is being continued to be developed and specific actions related to the continuation of the validation of the database by performing measurements of thermodynamic properties on complex compositions will be carried out in order to test the validity of the database and to further improve it. More widely, such computational tool will also have practical use in waste management and disposal, as well as in spent fuel storage applications.

Declaration of competing interest

The authors declare that they have no known competing financial interests or personal relationships that could have appeared to influence the work reported in this paper.

References

[1] D.R. Olander, Fundamental aspects of nuclear reactor fuel elements: prepared for the division of reactor development and demonstration, energy research and development administration, technical information center, office of public affairs, energy research and development Administration, National Technical Information Service, U.S. Dept. of Commerce, Oak Ridge, Springfield, 1976.

[2] H. Kleykamp, The chemical state of the fission products in oxide fuels, J. Nucl. Mater. 131 (1985) 221–246, https://doi.org/10.1016/0022-3115(85)90460-X.

[3] M.H.A. Piro, D. Sunderland, S. Livingstone, J. Sercombe, W. Revie, A. Quastel, K. Terrani, C. Judge, A review of pellet–clad interaction behavior in zirconium alloy fuel cladding, in: second ed., in: R.J.M. Konings, R.E. Stoller (Eds.), Comprehensive Nuclear Materials, vol. 2, Elsevier, 2019, pp. 248–306, https://doi.org/10.1016/B978-0-12-803581-8.09799-X.

[4] C. Gueneau, J.-C. Dumas, M.H.A. Piro, In Reactor behavior, in: M.H.A. Piro (Ed.), Advances in Nuclear Fuel Chemistry, Elsevier, 2020, pp. 419–467.

[5] R. Parrish, A. Aitkaliyeva, A review of microstructural features in fast reactor mixed oxide fuels, J. Nucl. Mater. 510 (2018) 644–660, https://doi.org/10.1016/j.jnucmat.2018.05.076.

[6] B. Baurens, J. Sercombe, C. Riglet-Martial, L. Desgranges, L. Trotignon, P. Maugis, 3D thermo-chemical–mechanical simulation of power ramps with ALCYONE fuel code, J. Nucl. Mater. 452 (2014) 578–594, https://doi.org/10.1016/j.jnucmat.2014.06.021.

[7] T.M. Besmann, J.W. McMurray, B.G. Gaston, S. Simunovic, M.H.A. Piro, Modeling thermochemistry of fuel and coupling to fuel performance codes, Proc, Top FUEL, 2016, p. 8.

[8] E. Skrzypek, M. Skrzypek, L. Saas, R. LeTellier, In vessel corium propagation sensitivity study of reactor pressure vessel rupture time with PROCOR platform, J. Power Technol 97 (2017) 110–116.

[9] Thermo-Calc Software, 2008. https://www.thermocalc.com/.

[10] Open Calphad Software. www.opencalphad.com/.

[11] H.L. Lukas, S.G. Fries, B. Sundman, Computational Thermodynamics: the CALPHAD Method, Cambridge University Press, 2007.

[12] Thermodynamics Advanced Fuels-International Database, OECD/NEA Joint Project, 2013. https://www.oecd-nea.org/science/taf-id/.

[13] C.R.C.T. FactSage, GTT. http://www.factsage.com/.

[14] W.T. Thompson, B.J. Lewis, E.C. Corcoran, M.H. Kaye, S.J. White, F. Akbari, Z. He, R. Verrall, J.D. Higgs, D.M. Thompson, T.M. Besmann, S.C. Vogel, Thermodynamic treatment of uranium dioxide based nuclear fuel, Int. J. Mater. Res. 98 (2007) 1004–1011, https://doi.org/10.3139/146.101556.

[15] M.H.A. Piro, J.-C. Dumas, B.J. Lewis, W.T. Thompson, F.C. Iglesias, Fission product chemistry in oxide fuels, in: second ed., in: R.J.M. Konings, R.E. Stoller (Eds.), Compr. Nucl. Mater., vol. 2, Elsevier, 2020, pp. 173–199, https://doi.org/10.1016/B978-0-12-803581-8.12048-X.

[16] M.H. Kaye, B.J. Lewis, W.T. Thompson, Thermodynamic treatment of noble metal fission products in nuclear fuel, J. Nucl. Mater. 366 (2007) 8–27, https://doi.org/10.1016/j.jnucmat.2006.11.014.

[17] E.H.P. Cordfunke, R.J.M. Konings, Thermochemical data for reactor materials and fission products: the ECN database, J. Phase Equil. 14 (1993) 457–464.

[18] E.H.P. Cordfunke, R.J.M. Konings, Thermochemical Data for Reactor Materials and Fission Products, Elsevier, 1990. Amsterdam.

[19] D. Shin, T.M. Besmann, Thermodynamic modeling of the $(U,La)O_{2\pm x}$ solid solution phase, J. Nucl. Mater. 433 (2013) 227–232, https://doi.org/10.1016/j.jnucmat.2012.09.009.

[20] J.W. McMurray, D. Shin, T.M. Besmann, Thermodynamic assessment of the U–La–O system, J. Nucl. Mater. 456 (2015) 142–150, https://doi.org/10.1016/j.jnucmat.2014.09.031.

[21] S.M. Lee, T.W. Knight, J.W. McMurray, T.M. Besmann, Measurement of the oxygen partial pressure and thermodynamic modeling of the U–Nd–O system, J. Nucl. Mater. 473 (2016) 272–282, https://doi.org/10.1016/j.jnucmat.2016.02.024.

[22] R.G. Brese, J.W. McMurray, D. Shin, T.M. Besmann, Thermodynamic assessment of the U–Y–O system, J. Nucl. Mater. 460 (2015) 5–12, https://doi.org/10.1016/j.jnucmat.2015.01.047.

[23] J.W. McMurray, D. Shin, B.W. Slone, T.M. Besmann, Thermochemical modeling of the $U_{1-y}Gd_yO_{2\pm x}$ phase, J. Nucl. Mater. 443 (2013) 588–595, https://doi.org/10.1016/j.jnucmat.2013.08.005.

[24] J.W. McMurray, D. Shin, B.W. Slone, T.M. Besmann, Thermodynamic reassessment of U–Gd–O system, J. Nucl. Mater. 452 (2014) 397–406, https://doi.org/10.1016/j.jnucmat.2014.04.047.

[25] J.W. McMurray, S. Hirooka, T. Murakami, K. Suzuki, J.T. White, S.L. Voit, A. T. Nelson, B.W. Slone, T.M. Besmann, K.J. McClellan, M. Kato, Thermodynamic assessment of the oxygen rich U–Ce–O system, J. Nucl. Mater. 467 (2015) 588–600, https://doi.org/10.1016/j.jnucmat.2015.10.008.

[26] J.W. McMurray, C.M. Silva, Experimental oxygen potentials for $U_{1-y}Pr_yO_{2\pm x}$ and thermodynamic assessment of the U-Pr-O system, J. Nucl. Mater. 470 (2016) 111–118, https://doi.org/10.1016/j.jnucmat.2015.11.059.

[27] C. Guéneau, S. Gossé, A. Quaini, N. Dupin, B. Sundman, M. Kurata, T. Besmann, P. E.A. Turchi, J.C. Dumas, E.C. Corcoran, M. Piro, T. Ogata, R. Hania, B.O. Lee, J. R. Kennedy, S. Massara, , FUELBASE, T.A.F.-I.D. Databases, OC Software, Advanced Computational Tools to Perform Thermodynamic Calculations on Nuclear Fuel Materials, Proceedings of the 7th European Review Meeting on Severe Accident Research (ERMSAR-2015), Marseille, France, 24-26 March 2015.

[28] M. Kurata, Thermodynamic database on U-Pu-Zr-Np-Am-Fe alloy system I — Re-evaluation of U-Pu-Zr alloy system -, IOP Conf. Ser. Mater. Sci. Eng. 9 (2010), 012022, https://doi.org/10.1088/1757-899X/9/1/012022.

[29] M. Kurata, Thermodynamic database on U-Pu-Zr-Np-Am-Fe alloy system II — evaluation of Np, Am, and Fe containing systems-, IOP Conf. Ser. Mater. Sci. Eng. 9 (2010), 012023, https://doi.org/10.1088/1757-899X/9/1/012023.

[30] M. Hillert, B. Jansson, B. Sundman, J. Ågren, A two-sublattice model for molten solutions with different tendency for ionization, Metall. Trans. A. 16 (1985) 261–266, https://doi.org/10.1007/BF02815307.

[31] B. Sundman, Modification of the two-sublattice model for liquids, Calphad 15 (1991) 109–119, https://doi.org/10.1016/0364-5916(91)90010-H.

[32] B. Sundman, J. Ågren, A regular solution model for phases with several components and sublattices, suitable for computer applications, J. Phys. Chem. Solid. 42 (1981) 297–301, https://doi.org/10.1016/0022-3697(81)90144-X.

[33] C. Guéneau, M. Baichi, D. Labroche, C. Chatillon, B. Sundman, Thermodynamic assessment of the uranium–oxygen system, J. Nucl. Mater. 304 (2002) 161–175, https://doi.org/10.1016/S0022-3115(02)00878-4.

[34] C. Guéneau, C. Chatillon, B. Sundman, Thermodynamic modelling of the plutonium–oxygen system, J. Nucl. Mater. 378 (2008) 257–272, https://doi.org/10.1016/j.jnucmat.2008.06.013.

[35] A. Berche, N. Dupin, C. Guéneau, C. Rado, B. Sundman, J.C. Dumas, Calphad thermodynamic description of some binary systems involving U, J. Nucl. Mater. 411 (2011) 131–143, https://doi.org/10.1016/j.jnucmat.2011.01.043.

[36] P. Gotcu-Freis, J.-Y. Colle, C. Guéneau, N. Dupin, B. Sundman, R.J.M. Konings, A thermodynamic study of the Pu–Am–O system, J. Nucl. Mater. 414 (2011) 408–421, https://doi.org/10.1016/j.jnucmat.2011.05.014.

[37] C. Guéneau, J.-L. Flèche, Thermodynamic assessment of the cesium–oxygen system by coupling density functional theory and CALPHAD approaches, Calphad 49 (2015) 67–78, https://doi.org/10.1016/j.calphad.2015.02.002.

[38] C. Guéneau, N. Dupin, B. Sundman, C. Martial, J.-C. Dumas, S. Gossé, S. Chatain, F. D. Bruycker, D. Manara, R.J.M. Konings, Thermodynamic modelling of advanced oxide and carbide nuclear fuels: description of the U–Pu–O–C systems, J. Nucl. Mater. 419 (2011) 145–167, https://doi.org/10.1016/j.jnucmat.2011.07.033.

[39] S. Gossé, N. Dupin, C. Guéneau, J.-C. Crivello, J.-M. Joubert, Thermodynamic assessment of the Pd-Rh-Ru system using calphad and first-principles methods, J. Nucl. Mater. 474 (2016) 163–173, https://doi.org/10.1016/j.jnucmat.2016.03.025.

[40] A. Berche, C. Rado, O. Rapaud, C. Guéneau, J. Rogez, Thermodynamic study of the U–Si system, J. Nucl. Mater. 389 (2009) 101–107, https://doi.org/10.1016/j.jnucmat.2009.01.014.

[41] T.-N. Pham Thi, J.-C. Dumas, V. Bouineau, N. Dupin, C. Guéneau, S. Gossé, P. Benigni, Ph Maugis, J. Rogez, Thermodynamic assessment of the Cs–Te binary system, Calphad 48 (2015) 1–12, https://doi.org/10.1016/j.calphad.2014.10.006.

[42] A. Berche, T. Alpettaz, S. Chatain, C. Blanc, S. Gossé, C. Guéneau, Thermodynamic study of the uranium-vanadium system, J. Chem. Thermodyn. 43 (2011) 458–466, https://doi.org/10.1016/j.jct.2010.10.023.

[43] S. Gossé, C. Guéneau, Thermodynamic assessment of the palladium-tellurium (Pd-Te) system, Intermetallics 19 (2011) 621–629, https://doi.org/10.1016/j.intermet.2010.12.014.

[44] E.C. Corcoran, J.-L. Flèche, N. Dupin, B. Sundman, C. Guéneau, Thermodynamic investigations of the uranium-molybdenum-oxygen system by a coupling of density functional theory and CALPAHD methodologies, Calphad 63 (2018) 196–211.

[45] A. Quaini, C. Guéneau, S. Gossé, N. Dupin, B. Sundman, E. Brackx, R. Domenger, M. Kurata, F. Hodaj, Contribution to the thermodynamic description of the corium – the U-Zr-O system, J. Nucl. Mater. 501 (2018) 104–131, https://doi.org/10.1016/j.jnucmat.2018.01.023.

[46] M. Kurata, Thermodynamic assessment of the Pu-U, Pu-Zr, and Pu-U-Zr systems, Calphad 23 (1999) 305–337, https://doi.org/10.1016/S0364-5916(00)00004-3.

[47] M. Kurata, Private Communication, 2006.

[48] P. Hofmann, KFK 2220 Report, 1976.

[49] C. Guéneau, V. Dauvois, P. Pérodeaud, O. Dugne, An experimental and theoritical thermodynamic approach to study the miscibility gap in a U-Zr-O-Fe model corium. Proc. MASCA Semin. 2004, NEA/OECD, Aix-en-Provence, France, 2004, pp. 299–320.

[50] MASCA NEA/OECD Joint Project, 2008. http://www.oecd-nea.org/jointproj/masca.html.

[51] S.V. Bechta, V.S. Granovsky, V.B. Khabensky, V.V. Gusarov, V.I. Almiashev, L. P. Mezentseva, E.V. Krushinov, S.Yu Kotova, R.A. Kosarevsky, M. Barrachin, D. Bottomley, F. Fichot, M. Fischer, Corium phase equilibria based on MASCA, METCOR and CORPHAD results, Nucl. Eng. Des. 238 (2008) 2761–2771, https://doi.org/10.1016/j.nucengdes.2008.04.018.

[52] M.F. Roche, L. Leibowitz, J.K. Fink, Baker Jr., Solidus and Liquidus Temperatures of Core-Concrete Mixtures, NUREG/CR-6032, 1993. ANL-93/9.

[53] A. Quaini, C. Guéneau, S. Gossé, T. Alpettaz, E. Brackx, R. Domenger, A. Chocard, F. Hodaj, Experimental contribution to the corium thermodynamic modelling - the U-Zr-Al-Ca-Si-O system, Ann. Nucl. Energy 93 (2016) 43–49, https://doi.org/10.1016/j.anucene.2016.01.043.

[54] L. Brissonneau, H. Ikeuchi, P. Piluso, J. Gousseau, C. David, V. Testud, J. Roger, V. Bouter, T. Kitagaki, A. Nakayoshi, S. Dubois, T. Washiya, Material characterization of theVULCANO corium concrete interaction test with concrete representative of Fukushma Daiichi Nuclear Plants, J. Nucl. Mater. 528 (2020) 151860.

[55] Hj Matzke, J. Ottaviani, D. Pellottiero, J. Rouault, Oxygen potential of high burn-up fast breeder oxide fuel, J. Nucl. Mater. 160 (1988) 142–146, https://doi.org/10.1016/0022-3115(88)90041-4.

[56] A. Tsilanizara, C.M. Diop, B. Nimal, M. Detoc, L. Lunéville, M. Chiron, T.D. Huynh, I. Brésard, M. Eid, J.C. Klein, B. Roque, P. Marimbeau, C. Garzenne, J.M. Parize, C. Vergne, Darwin: an evolution code system for a large range of applications, J. Nucl. Sci. Technol. 37 (2000) 845–849, https://doi.org/10.1080/00223131.2000.10875009.

[57] L. San-Felice, R. Eschbach, P. Bourdot, A. Tsilanizara, in: Knoxville (Ed.), Experimental Validation of the Darwin2.3 Package for Fuel Cycle Applications, Tennessee, USA, 2012.

[58] Y. Guerin, 2.21 - fuel performance of fast spectrum oxide fuel, in: R.J.M. Konings (Ed.), Compr. Nucl. Mater., Elsevier, Oxford, 2012, pp. 547–578, https://doi.org/10.1016/B978-0-08-056033-5.00043-4.

[59] S. Imoto, Chemical state of fission products in irradiated UO_2, J. Nucl. Mater. 140 (1986) 19–27, https://doi.org/10.1016/0022-3115(86)90192-3.

[60] T. Muromura, T. Adachi, H. Takeishi, T. Yamamoto, Metallic phases precipitated in UO2 fuel : II Onsoluble residue in simulated fuel, J. Nucl. Mater. 160 (1988) 318–326.

[61] R.J. Parrish, K.E. Wright, A.J. Winston, C. McKinney, J.M. Harp, A. Aitkaliyeva, Characterization of solid fission products in 13.7 % FIMA MOX fuel using electron microscopy techniques, J. Nucl. Mater. 524 (2019) 67–79.

[62] H. Kleykamp, Post-irradiation studies on the $(U,Pu)O_2$ cluster experiment POUSSIX in the PHENIX reactor, Forschungszentrum Karslruhe, 2001. Report FZKA 6679.

[63] H. Kleykamp, J.O. Paschoal, R. Pejsa, F. Thommler, Composition and structure of fission product precipitates in irradiated oxide fuels : correlation with phase studies in the Mo-Ru-Rh-Pd and $BaO-UO_2-ZrO_2-MoO_2$ systems, J. Nucl. Mater. 130 (1985) 426–433.

[64] K. Samuelson, J.-C. Dumas, B. Sundman, J. Lamontagne, C. Guéneau, Simulation of the chemical state of high burnup $(U,Pu)O_2$ fuel in fast reactors based on thermodynamic calculations, J. Nucl. Mater. 532 (2020) 151969.

[65] K. Samuelsson, J.-C. Dumas, B. Sundman, M. Lainet, An improved method to evaluate the « Joint Oxyde-Gaine » formation in $(U,Pu)O_2$ irradiated fuels using the GERMINAL V2 code coupled to Calphad thermodynamic computations, EPJ Nuclear Sci. Technol. 6 (2020) 47, 10:1051/epjn/2020008.

[66] T. Hirosawa, I. Sato, Burnup dependence of melting temperature of FBR mixed oxide fuels irradiated to high burnup, J. Nucl. Mater. 418 (2011) 202–214.

[67] L. Burris, H.M. Feder, S. Lawroski, W.A. Rodger, R.C. Vogel, The melt refining of irradiated uranium: application to EBR-II fast reactor fuel. I. Introduction, Nucl. Sci. Eng. 6 (6) (1959) 493–495, https://doi.org/10.13182/NSE59-A15507.

[68] G.L. Hofman, L.C. Walters, T.H. Bauer, Metallic fast reactor fuels, Prog. Nucl. Energy 31 (1997) 83–110, https://doi.org/10.1016/0149-1970(96)00005-4.

[69] J.M. Harp, L. Capriotti, D.L. Porter, J.I. Cole, U-10Zr and U-5Fs: fuel/cladding chemical interaction behavior differences, J. Nucl. Mater. 528 (2020) 151840, https://doi.org/10.1016/j.jnucmat.2019.151840.

[70] M.H.A. Piro, B.W. Leitch, Conjugate heat transfer simulations of advanced research reactor fuel, Nucl. Eng. Des. 274 (2014) 30–43, https://doi.org/10.1016/j.nucengdes.2014.03.054.

[71] J. Gan, D.D. Keiser, B.D. Miller, J.F. Jue, A.B. Robinson, J. Madden, TEM characterization of irradiated U-7Mo/Mg dispersion fuel, J. Nucl. Mater. 494 (2017) 380–397, https://doi.org/10.1016/j.jnucmat.2017.07.030.

[72] M.K. Meyer, D.D. Keiser Jr., J.-F. Jue, E. Shaber, Research reactor fuels, in: M.H. A. Piro (Ed.), Advances in Nuclear Fuel Chemistry, Elsevier, 2020, pp. 273–312.

[73] H.-J. Ryu, Y.-S. Kim, J.-M. Park, H.-T. Chae, C.-K. Kim, Performance evaluation of u-mo/al dispersion fuel by considering a fuel-matrix interaction, Nucl. Eng. Technol. 40 (2008) 409–418, https://doi.org/10.5516/NET.2008.40.5.409.

[74] D.F. Sears, B.W. Leitch, G.W. Edwards, K. Colon, I.P. Swainson, R.B. Rogge, R. L. Donaberger, Effect of burnup and irradiation temperature on crystalline phase evolution in Al/U-Mo dispersion fuel, Proc Inter Mtg RERTR, Beijing, China, 2009.

[75] J. Wang, X.J. Liu, C.P. Wang, Thermodynamic modeling of the Al–U and Co–U systems, J. Nucl. Mater. 374 (2008) 79–86, https://doi.org/10.1016/j.jnucmat.2007.06.023.

[76] L. Xiao, N. Wang, Growth behavior of intermetallic compounds during reactive diffusion between aluminum alloy 1060 and magnesium at 573–673K, J. Nucl. Mater. 456 (2015) 389–397, https://doi.org/10.1016/j.jnucmat.2014.09.022.

[77] N. Saunders, A review and thermodynamic assessment of the Al-Mg and Mg-Li systems, Calphad 14 (1990) 61–70, https://doi.org/10.1016/0364-5916(90)90040-7.

[78] P. Liang, H.L. Su, P. Donnadieu, M.G. Harmelin, A. Quivy, G. Effenberg, H. J. Seifert, H.L. Lukas, F. Aldinger, Z. Met. 89 (1998) 536–540.

[79] M. Kulakov, M. Saoudi, M.H.A. Piro, R.L. Donaberger, Structure and thermal properties of as-fabricated U-7Mo/Mg and U-10Mo/Mg low-enriched uranium research reactor fuels, J. Nucl. Mater. 484 (2017) 288–296, https://doi.org/10.1016/j.jnucmat.2016.12.005.

[80] E. Moore, C. Guéneau, J.-P. Crocombette, Diffusion model of the non-stoichiometric uranium dioxide, J. Solid State Chem. 203 (2013) 145–153, https://doi.org/10.1016/j.jssc.2013.04.006.

[81] E. Moore, C. Guéneau, J.-P. Crocombette, Oxygen diffusion model of the mixed $(U,Pu)O_{2\pm x}$: assessment and application, J. Nucl. Mater. 485 (2017) 216–230, https://doi.org/10.1016/j.jnucmat.2016.12.026.

[82] M.J. Welland, E. Tenuta, A.A. Prudil, Linearization-based method for solving a multicomponent diffusion phase-field model with arbitrary solution thermodynamics, Phys. Rev. E. 95 (2017), 063312, https://doi.org/10.1103/PhysRevE.95.063312.

[83] M.J. Welland, M.H.A. Piro, S. Hibbins, N. Wang, A method of integrating CALPHAD data into phase-field models using an approximated minimiser applied to intermetallic layer growth in the Al-Mg system, Calphad 59 (2017) 76–83, https://doi.org/10.1016/j.calphad.2017.07.008.

[84] M. Plapp, Unified derivation of phase-field models for alloy solidification from a grand-potential functional, Phys. Rev. E. 84 (2011), 031601, https://doi.org/10.1103/PhysRevE.84.031601.

[85] M.H.A. Piro, M.J. Welland, M. Stan, On the interpretation of chemical potentials computed from equilibrium thermodynamic codes, J. Nucl. Mater. 464 (2015) 48–52, https://doi.org/10.1016/j.jnucmat.2015.04.004.

[86] R.L. Williamson, J.D. Hales, S.R. Novascone, M.R. Tonks, D.R. Gaston, C. J. Permann, D. Andrs, R.C. Martineau, Multidimensional multiphysics simulation of nuclear fuel behavior, J. Nucl. Mater. 423 (2012) 149–163, https://doi.org/10.1016/j.jnucmat.2012.01.012.

[87] M.H.A. Piro, S. Simunovic, T.M. Besmann, B.J. Lewis, W.T. Thompson, The thermochemistry library Thermochimica, Comput. Mater. Sci. 67 (2013) 266–272, https://doi.org/10.1016/j.commatsci.2012.09.011.

[88] S. Simunovic, T.M. Besmann, E. Moore, M. Poschmann, M.H.A. Piro, K.T. Clarno, J. W. McMurray, W.A. Weiselquist, Modeling and simulation of oxygen transport in high burnup LWR fuel, J. Nucl. Mater. 538 (2020) 152194, https://doi.org/10.1016/j.jnucmat.2020.152194.